

Multilayered triangular and quadrilateral flat shell elements based on the Refined Zigzag Theory

Original

Multilayered triangular and quadrilateral flat shell elements based on the Refined Zigzag Theory / Gherlone, M.; Versino, D.; Zarra, V.. - In: COMPOSITE STRUCTURES. - ISSN 0263-8223. - ELETTRONICO. - 233:(2020), p. 111629. [10.1016/j.compstruct.2019.111629]

Availability:

This version is available at: 11583/2781992 since: 2020-01-17T15:38:25Z

Publisher:

Elsevier Ltd

Published

DOI:10.1016/j.compstruct.2019.111629

Terms of use:

This article is made available under terms and conditions as specified in the corresponding bibliographic description in the repository

Publisher copyright

Elsevier postprint/Author's Accepted Manuscript

© 2020. This manuscript version is made available under the CC-BY-NC-ND 4.0 license
<http://creativecommons.org/licenses/by-nc-nd/4.0/>. The final authenticated version is available online at:
<http://dx.doi.org/10.1016/j.compstruct.2019.111629>

(Article begins on next page)

Multilayered triangular and quadrilateral flat shell elements based on the Refined Zigzag Theory

Marco Gherlone^{a}, Daniele Versino^b and Vincenzo Zarra^a*

*^a Department of Mechanical and Aerospace Engineering, Politecnico di Torino,
Corso Duca degli Abruzzi 24, 10129, Torino, Italy*

*^b Theoretical Division T-3, Los Alamos National Laboratory,
Mail Stop B216, Los Alamos, New Mexico 87545, USA*

** Corresponding author. Tel.: +39 011 090 6817; fax: +39 011 090 6999
E-mail address: marco.gherlone@polito.it*

ABSTRACT

The paper presents a class of C^0 -continuous, flat shell elements based on the Refined Zigzag Theory (RZT) for the analysis of multilayered and curved composite and sandwich structures. The use of the interdependent interpolation strategy allows eliminating the shear-locking phenomenon and introducing the drilling rotation necessary to complete the set of classical nodal degrees of freedom (three displacements and three rotations). Additional kinematic variables are present in RZT, the zigzag rotations around the in-plane axes that measure the normal distortion typical of multilayered structures. An additional “drilling” zigzag rotation is therefore included among the nodal degrees of freedom in order to properly model curved and built-up structures. A stabilization procedure is adopted to suppress spurious zero-energy modes. A three-node triangular and a four-node quadrilateral flat shell element are formulated

with 9 degrees of freedom per node. Example problems involving flat and curved multilayered structures are presented and discussed in order to assess the accuracy and convergence properties of the presented elements. Both static response predictions and free vibrations analyses are considered and the comparison is made with analytic RZT solutions, high-fidelity 3D finite element models and FSDT-based flat shell elements.

KEYWORDS

Layered Structures, Curved Structures, Built-up Structures, Refined Zigzag Theory, Finite Elements, Shear Locking, Drilling Rotation

1. INTRODUCTION

Open literature presents a great number of papers dealing with the analysis of multilayered composite and sandwich structures and the topic is still nowadays investigated by many authors. On one hand, the interest in composite materials and layered structures is due to their excellent specific properties (stiffness-to-weight and strength-to-weight) and to the possibility to tailor the mechanical behavior of the component depending on the application. On the other hand, some peculiarities of multilayered composite structures (transverse shear deformability, through-the-thickness anisotropy) require accurate approaches to reconstruct the structural response. The traditional approach for the analysis of multilayered structures is based on kinematic assumptions that lead to a displacements field. Strains and stresses are consistently derived and the governing equations are obtained using the Principle of Virtual Works (PVW) [1,2]. When the assumptions on the displacements field are valid along the whole thickness, Equivalent Single Layer (ESL) theories are obtained (refer to [3] for a review of ESL theories based on displacement unknowns). Among these, the

Classical Lamination Theory (CLT) based on Kirchhoff's hypotheses [4] and the First-order Shear Deformation Theory (FSDT) [5-7] have to be considered. These simple approaches provide good response predictions for thin plates with limited transverse anisotropy. The accuracy of FSDT can be improved and its range of applicability can be extended to moderately thick composite structures if ad hoc transverse shear correction factors are used [8]. Nevertheless, it has been shown that the correction is not always effective, especially for sandwich structures with high face-to-core stiffness and thickness ratios [9]. In order to take into account the transverse shear deformability effect (especially when moderately thick and thick shell structures are analyzed), high-order theories have been developed [10-18]. Nevertheless, these theories are not able to guarantee the through-the-thickness continuity of transverse shear and normal stresses when obtained from the constitutive equations and the integration of Cauchy's indefinite equilibrium equations is often invoked as a "corrector" procedure. A further enhancement can be achieved by formulating Layer-Wise (LW) theories where the displacements field is assumed in each layer [19,20]. This provides sufficient through-the-thickness kinematic freedom and allows, in some cases, to enforce the transverse shear stresses to be continuous [20]. The drawback relies in the computational complexity that increases with the number of physical layers. A compromise between ESL and LW approaches is represented by the zigzag theories pioneered by Di Sciuva [21-24] and further developed by Cho [25], Averill [26,27] and Icardi [28,29]. The number of kinematic variables is fixed as in ESL theories and the transverse shear stresses are set to be through-the-thickness continuous as in LW theories, thus leading to accurate response predictions at an affordable computational cost. A recent development in the framework of zigzag theories is represented by the Refined Zigzag Theory that has been formulated for beams [30] and plates [31] and then assessed on a

wide spectrum of material systems, ranging from homogenous [32] to multilayered sandwich [9], functionally-graded plates [33,34] and functionally-graded carbon nanotube-reinforced sandwich plates [35].

An alternative approach is based on the a priori assumption of the through-the thickness distribution of displacements and transverse stresses and on the use of the Reissner's Mixed Variational Theorem (RMVT) [36]. Transverse stresses can be therefore easily assumed to be continuous. Several papers have been presented within this framework [37], starting from the first ones by Murakami (ESL theory proposed in [38] and LW approach proposed in [39]). A recent mixed version of RZT (called RZT^(m)) has been formulated for both beam [40] and plate [41] structures.

For further discussions and for a broader review on theories for the analysis of multilayered composite and sandwich structures, in particular zigzag theories, refer to [1-3,10,11,37,42-44].

Since RZT and RZT^(m) may be regarded as an enrichment of FSDT, they suffer from the same shear-locking phenomenon that affect FSDT-based finite elements in the thin regime, i.e., when very slender beams or thin plates are modeled with finite elements [45]. Among the several strategies proposed to overcome shear locking in FSDT finite elements, the so-called interdependent interpolation strategy is based on the approximation of the deflection with polynomials one order higher than polynomials used for bending rotations [46], thus obtaining internal nodes where only deflection degrees of freedom are defined. This approach has been first proposed for Timoshenko beam finite elements [46] and then extended to FSDT quadrilateral [47] and triangular [48] plate finite elements. The element topology can be simplified with appropriate constraining conditions [46]. Similarly, the interdependent interpolation strategy has

been applied (with an improved constraining condition) to beam elements based on RZT [45,49] and $RZT^{(m)}$ [50] and to plate elements based on RZT [51] and $RZT^{(m)}$ [52].

In engineering applications involving thick and thin multilayered structures, it is highly desirable to have efficient finite elements able to yield accurate solutions when curved surfaces are modeled or coupling between shell and beam elements is required. While curved degenerated shell elements based on the Naghdi displacement field [53], although very effective, introduce additional complexity to the finite element formulation that leads to an increased computational cost, flat shell elements offer a good balance between performances, formulation simplicity and computational cost. When a general purpose FSDT-based shell finite element is developed, it is necessary to equip each node with six mechanical degrees of freedom: three displacements and three rotations. Since FSDT defines only the rotations around the two in-plane axes, it is not possible to associate a stiffness to the rotation around the normal axis (also known as drilling rotation). In literature several strategies that address this issue have been proposed and these methods may be classified in four classes according to the fact that are based on (1) adding a fictitious stiffness to the drilling rotation [54-56], (2) enhancing the strain field with non-conforming modes [57,58], (3) modifying the variational statement by bringing in an additional term related to the rotation around the element's normal [59-62] (4) introducing the drilling rotation at the shape-function level [63-69].

In particular, in [67,68], the elimination of shear locking and the introduction of the drilling rotation are addressed together for plate elements based on FSDT [67] and on his {1,2} theory by Tessler [68]. The approach consists of considering any plate element's edge as a Timoshenko beam in a 3D space and deriving the shape functions starting from quadratic and linear polynomials that interpolate the displacements and

rotations, respectively. Consequently to this particular choice, three issues are solved at the same time: 1) according to the interdependent interpolation scheme [46-48], the shear locking is relieved since the deflection interpolation is one order higher than the rotation interpolation 2) the quadratic displacement field allows for full displacement compatibility between non co-planar adjacent elements [68] 3) a drilling rotation is introduced at the shape-function level obtaining a formulation that is very similar to the Allman-type shape functions [63,64].

This paper is concerned with the development of RZT-based triangular and quadrilateral flat shell elements with drilling degree of freedom formulation, suitable for linear static analysis and modal analysis of multilayered composite and sandwich structures. The dynamic version of the virtual work principle is employed to obtain a variationally consistent formulation. A full-integration scheme is employed since the shear locking has been removed with the interdependent interpolation and a stabilization matrix is adopted to remove the zero energy modes introduced with the drilling degree of freedom. Furthermore, a “drilling” component of the zigzag rotation is introduced as nodal degree of freedom. Convergence and accuracy of the proposed shell elements are preliminarily assessed considering the static response of flat multilayered plates and, subsequently, through numerical experiments involving linear static response and free vibrations of curved sandwich structures.

2. REFINED ZIGZAG THEORY

In this section, the Refined Zigzag Theory is briefly described in order to set the framework for the flat shell finite elements development. For a complete and detailed discussion on RZT for plates, refer to [31].

2.1 Displacements, strains and stresses

In a global three-dimensional Cartesian coordinate system defined by the coordinate axis (X, Y, Z) , a flat linear elastic multilayered shell is considered. The shell is equipped with a local orthonormal reference frame (x_1, x_2, z) where the orthogonal axes (x_1, x_2) define the shell's mid-plane, S , and z is the thickness coordinate ranging from $-h$ to $+h$. The total laminate thickness is $2h$ and $z=0$ denotes the mid-plane of the shell (Figure 1). The laminate is made of N perfectly bonded orthotropic layers; the k -th layer is denoted with the superscript (k) .

The displacement field of RZT referred to the (x_1, x_2, z) coordinate system,

$\mathbf{s} \equiv [u_1^{(k)} \quad u_2^{(k)} \quad u_z]^T$, can be thus written as follows [31]

$$\begin{aligned} u_1^{(k)}(x_1, x_2, z) &= u(x_1, x_2) + z\theta_1(x_1, x_2) + \phi_1^{(k)}(z)\psi_1(x_1, x_2) \\ u_2^{(k)}(x_1, x_2, z) &= v(x_1, x_2) + z\theta_2(x_1, x_2) + \phi_2^{(k)}(z)\psi_2(x_1, x_2) \\ u_z(x_1, x_2, z) &= w(x_1, x_2) \end{aligned} \quad (1)$$

with the following definition of the seven kinematic variables,

$\mathbf{u} \equiv [u \quad v \quad w \quad \theta_1 \quad \theta_2 \quad \psi_1 \quad \psi_2]^T$ (Figure 1): u , v , and w are the uniform

displacement components along the x_1 -, x_2 -, and z -axis respectively (u and v are the in-plane displacements while w is the transverse deflection); θ_1 and θ_2 are the bending rotations of the transverse normal around the positive x_2 -axis and the negative x_1 -axis, respectively; ψ_1 and ψ_2 are the zigzag rotations around the positive x_2 - and negative x_1 -direction, respectively, and measure the magnitude of the zigzag effect, i.e., the distortion of the normal typical of multilayered structures. The through-the-thickness pattern of the normal distortion is modeled by the zigzag functions $(\phi_1^{(k)}, \phi_2^{(k)})$ which depend on the thickness and on the transverse shear modulus of each layer. For a

complete discussion of the zigzag rotations and a detailed derivation of the zigzag functions, refer to [31].

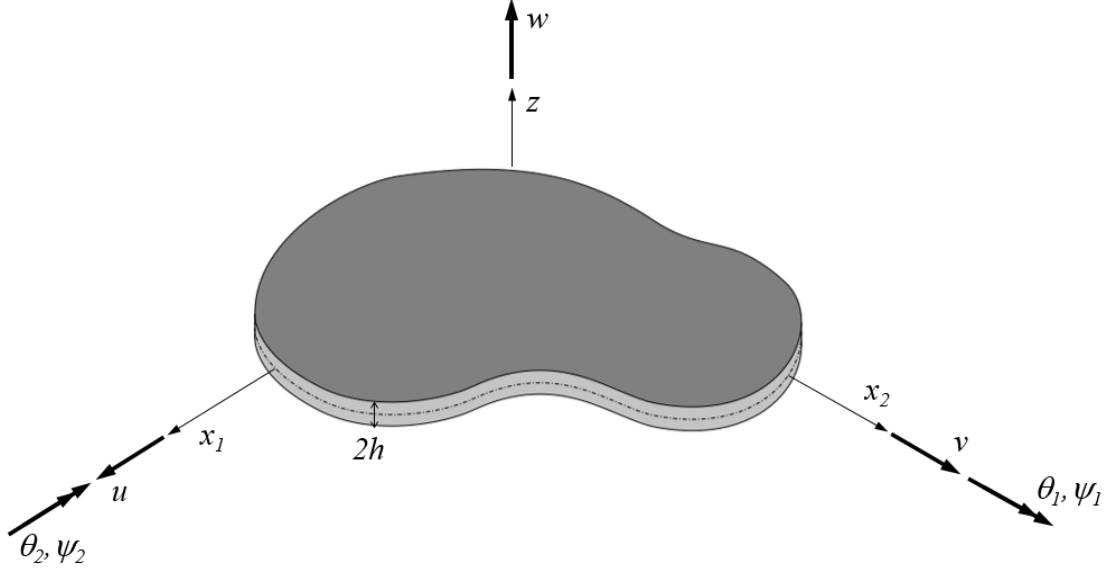


Figure 1. Plate geometry and notation for Refined Zigzag Theory.

Using the linear strain-displacement relations, the in-plane and transverse shear strains become

$$\begin{aligned}
 \varepsilon_{11}^{(k)} &= u_{,1} + z\theta_{1,1} + \phi_1^{(k)}\psi_{1,1} \\
 \varepsilon_{22}^{(k)} &= v_{,2} + z\theta_{2,2} + \phi_2^{(k)}\psi_{2,2} \\
 \gamma_{12}^{(k)} &= u_{,2} + v_{,1} + z(\theta_{1,2} + \theta_{2,1}) + \phi_1^{(k)}\psi_{1,2} + \phi_2^{(k)}\psi_{2,1} \\
 \gamma_{1z}^{(k)} &= \gamma_1 + \beta_1^{(k)}\psi_1 \\
 \gamma_{2z}^{(k)} &= \gamma_2 + \beta_2^{(k)}\psi_2
 \end{aligned} \tag{2}$$

where $\gamma_\alpha \equiv w_{,\alpha} + \theta_\alpha$ and $\beta_\alpha^{(k)} \equiv \phi_{\alpha,z}^{(k)}$ ($\alpha=1,2$). The in-plane and transverse shear

components of the strain field can be represented using the vectors

$\boldsymbol{\varepsilon} \equiv [\varepsilon_{11}^{(k)} \quad \varepsilon_{22}^{(k)} \quad \gamma_{12}^{(k)}]^T$ and $\boldsymbol{\gamma} \equiv [\gamma_{1z}^{(k)} \quad \gamma_{2z}^{(k)}]^T$, respectively. The corresponding in-plane

and transverse shear stress components, $\boldsymbol{\sigma} \equiv [\sigma_{11}^{(k)} \quad \sigma_{22}^{(k)} \quad \tau_{12}^{(k)}]^T$ and $\boldsymbol{\tau} \equiv [\tau_{1z}^{(k)} \quad \tau_{2z}^{(k)}]^T$,

can be calculated through the constitutive equations

$$\begin{aligned}\boldsymbol{\sigma} &= \mathbf{C}\boldsymbol{\varepsilon} \\ \boldsymbol{\tau} &= \mathbf{Q}\boldsymbol{\gamma}\end{aligned}\tag{3}$$

where $\mathbf{C} \equiv [C_{ij}^{(k)}]$ ($i, j = 1, 2, 6$) and $\mathbf{Q} \equiv [Q_{\alpha\beta}^{(k)}]$ ($\alpha, \beta = 1, 2$) are the matrices of transformed reduced elastic stiffness coefficients in the (x_1, x_2, z) coordinate system, and relative to the plane-stress condition that ignores the transverse-normal stress.

2.2 Governing equations

The governing equations for RZT can be obtained from the D'Alembert's Principle

$$\int_V (\delta \boldsymbol{\varepsilon}^T \boldsymbol{\sigma} + \delta \boldsymbol{\gamma}^T \boldsymbol{\tau}) dV = - \int_V \delta \mathbf{s}^T \rho \ddot{\mathbf{s}} dV + \delta W_e \tag{4}$$

where V is the volume of the plate, W_e is the work of external loads and ρ is the mass density. Substituting Eqs. (1)-(3) into Eq. (4) and then integrating over the thickness coordinate, yields

$$\int_S (\delta \mathbf{e}_m^T \mathbf{A} \mathbf{e}_m + \delta \mathbf{e}_m^T \mathbf{B} \mathbf{e}_b + \delta \mathbf{e}_b^T \mathbf{B}^T \mathbf{e}_m + \delta \mathbf{e}_b^T \mathbf{D} \mathbf{e}_b + \delta \mathbf{e}_s^T \mathbf{G} \mathbf{e}_s) dS = - \int_S \delta \mathbf{u}^T \boldsymbol{\Gamma} \ddot{\mathbf{u}} dS + \delta W_e \tag{5}$$

where: \mathbf{e}_m , \mathbf{e}_b , \mathbf{e}_s are the RZT strain measures; \mathbf{A} , \mathbf{B} , \mathbf{D} , \mathbf{G} are the corresponding RZT stiffness coefficients matrices; $\boldsymbol{\Gamma}$ is the RZT inertia coefficients matrix (refer to the Appendix A for the complete definition).

The Euler-Lagrange equations of motion for RZT and the related set of consistent boundary conditions can be derived from Eq. (5) by performing integration by parts (refer to [9] for the details of the derivation).

It is now possible to formulate variationally consistent flat shell finite elements starting from Eq. (5) and employing C^0 -continuous shape functions for the interpolation of the kinematic variables since their maximum differentiation order with respect to the spatial variables is one in the strain components, Eqs. (2).

3. RZT FLAT SHELL ELEMENTS FORMULATION

Starting from Eq. (5), the equations of motion can be derived at the element level in terms of the element mass matrix, stiffness matrix and load vector by introducing the appropriate approximation of the kinematic variables. The shape functions choice is a key point for the development of computationally efficient RZT-based finite elements since this class of finite elements is proven to be affected by shear locking [45,51] and it is hence necessary to resort to appropriate strategies to relieve the element formulation of this phenomenon.

Within the spirit of what has been done in [51,52], the shear locking is removed employing an enhanced version of the interdependent interpolation strategy formulated by Tessler in [67]. In [67] Tessler developed a triangular shell element based on FSDT, employing the interdependent interpolation strategy to overcome the shear locking; quadratic shape functions were used for the deflection as well as for the in-plane displacements whereas linear shape functions were used for the bending rotations. Besides solving the shear locking issue, this approach allows to introduce the drilling degrees of freedom, to obtain a fully compatible displacement field at the interface between two adjacent elements while improving the element performances in

membrane-dominated problems. In order to minimize the number of nodal unknowns, two different constraining strategies were employed to condense-out the additional degrees of freedom introduced with the quadratic approximation. The aforementioned constraints are enforced locally on each edge of the triangular element considered as a Timoshenko beam [67]. The triangular shell element is finally assembled by joining the three beams thus resulting in a beam-frame in a three-dimensional Cartesian coordinate system.

In order to adapt this procedure to RZT, before introducing the triangular and quadrilateral shell finite element formulation, it is thus necessary to develop, in a three-dimensional reference frame, an RZT-based beam finite element with quadratic displacements and eventually, by means of the appropriate constraining strategies, reduce the number of nodal unknowns.

3.1 3D deformation of RZT-based beam element

A local orthonormal reference frame (r, s, n) is built up on a straight, linear elastic, multilayered composite beam of length L such as the r – axis is normal to the cross section and runs from the node 1 to the node 2, the n – axis is directed along the through-the-thickness layered direction and the s – axis completes the right-handed orthogonal reference frame (Figure 2). The beam's displacement field based on RZT can hence be expressed, with respect to the local coordinate system, in terms of six independent kinematic variables

$$\begin{aligned} u_r^{(k)}(r, s, n) &\equiv u_r(r) + n\theta_s(r) - s\theta_n(r) + \phi^{(k)}(n)\psi_s(r) \\ u_s(r, s, n) &\equiv u_s(r) \\ u_n(r, s, n) &\equiv u_n(r) \end{aligned} \tag{6}$$

where u_r , u_s and u_n are the uniform displacements components along the three coordinate axes; θ_s and ψ_s are the bending and zigzag rotations around the positive s – axis; θ_n is the bending rotation around the positive n – axis; $\phi^{(k)}$ is the zigzag function of the k – th layer (Figure 2).

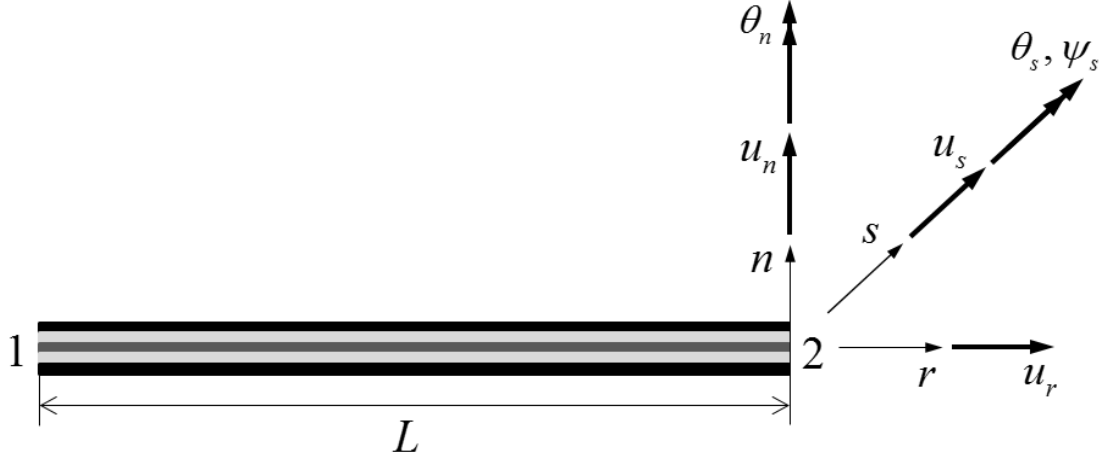


Figure 2. RZT-based beam finite element: topology and kinematic variables.

Although, by analogy with the rotation θ_n , the zigzag rotation ψ_n around the n – axis may be expected to exist as well, it has to be observed that ψ_n would not have any physical meaning since the beam is laminated along the n – axis only. From the Green-Cauchy definitions, the in-plane shear strain, γ_{rs} , is derived as follows

$$\gamma_{rs} \equiv \frac{\partial u_r^{(k)}}{\partial s} + \frac{\partial u_s^{(k)}}{\partial r} = -\theta_n + u_{s,r} \quad (7)$$

whereas, for the transverse shear strain, the RZT measure [30,45], η_m , is considered

$$\eta_m \equiv \theta_s + u_{n,r} - \psi_s \quad (8)$$

3.2 Three-node 15-dofs unconstrained beam element

A three-node beam finite element is presented first. According to the interdependent interpolation strategy, the displacement variables have to be approximated with a polynomial one order higher than the rotation kinematic variables; therefore, the displacements u_r , u_s and u_n are approximated with parabolic shape functions while for the bending and zigzag rotations, θ_s , θ_n , ψ_s , linear shape functions are employed

$$u_r(r) = \sum_{\ell} u_{r\ell} P_{\ell}(r) \quad u_s(r) = \sum_{\ell} u_{s\ell} P_{\ell}(r) \quad u_n(r) = \sum_{\ell} u_{n\ell} P_{\ell}(r) \quad (9)$$

$$\theta_s(r) = \sum_i \theta_{si} L_i(r) \quad \theta_n(r) = \sum_i \theta_{ni} L_i(r) \quad \psi_s(r) = \sum_i \psi_{si} L_i(r) \quad (10)$$

with $i = 1, 2$, $\ell = 1, m, 2$ and with the interpolation polynomials given by

$$L_i = [L_1, L_2] = \left[\frac{1}{2}(1-\xi), \frac{1}{2}(1+\xi) \right] \quad (11)$$

$$P_{\ell} = [P_1, P_m, P_2] = \left[\frac{1}{2}(\xi-1)\xi, (1-\xi^2), \frac{1}{2}(1+\xi)\xi \right]$$

where the non-dimensional longitudinal coordinate $\xi \equiv 2r/L \in [-1, 1]$ has been introduced. The unconstrained beam element has a total of 15 nodal degrees of freedom, three for each displacement and two for each rotation (Figure 3).

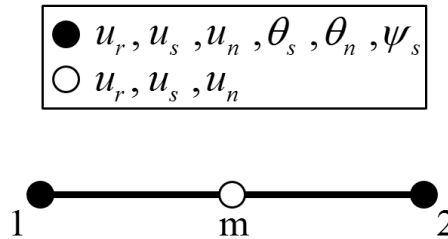


Figure 3. Unconstrained RZT-based beam finite element: topology and nodal degrees of freedom.

3.3 Two-node 12-dofs constrained beam element

In order to condense-out the mid-node displacement degrees of freedom, three assumptions on the displacements and strains are made. The first constraint is obtained by imposing that the axial displacement u_r is linear with respect to the axial direction [63,64,67,68]

$$\frac{\partial^2 u_r}{\partial r^2} = 0 \quad (12)$$

The other two conditions are derived by applying the interdependent interpolation strategy, i.e., enforcing the constancy of the in-plane shear strain, Eq. (7), and RZT transverse shear strain measure, Eq. (8), with respect to the axial coordinate r

$$\begin{aligned} \frac{\partial \gamma_{rs}}{\partial r} &= 0 \\ \frac{\partial \eta_m}{\partial r} &= 0 \end{aligned} \quad (13)$$

It should be noted that the second condition of Eq. (13) has been proven to be very effective [45,51] and to produce more accurate results for thick and thin laminates with respect to other constraining conditions.

After introducing the kinematic variables interpolation, Eqs. (9) and (10), into Eqs. (7) and (8) and then using Eqs. (12) and (13), the displacements of the mid-node m are written as

$$\begin{aligned}
u_{rm} &= \frac{1}{2}(u_{r1} + u_{r2}) \\
u_{sm} &= \frac{1}{2}(u_{s1} + u_{s2}) - \frac{L}{8}(\theta_{n2} - \theta_{n1}) \\
u_{nm} &= \frac{1}{2}(u_{n1} + u_{n2}) + \frac{L}{8}(\theta_{s2} - \theta_{s1}) - \frac{L}{8}(\psi_{s2} - \psi_{s1})
\end{aligned} \tag{14}$$

Substituting Eqs. (14) into Eqs. (9) results in an interpolation scheme that is different from the original one (Eqs. (9) and (10)) only for the displacements

$$\begin{aligned}
u_r(r) &= \sum_i u_{ri} L_i(r) \\
u_s(r) &= \sum_i u_{si} L_i(r) - \frac{L}{8}(\theta_{n2} - \theta_{n1}) P_m(r) \\
u_n(r) &= \sum_i u_{ni} L_i(r) + \frac{L}{8}(\theta_{s2} - \theta_{s1}) P_m(r) - \frac{L}{8}(\psi_{s2} - \psi_{s1}) P_m(r)
\end{aligned} \tag{15}$$

Finally, the constrained beam element has a total of twelve nodal degrees of freedom, two for each displacement and rotation (Figure 4).

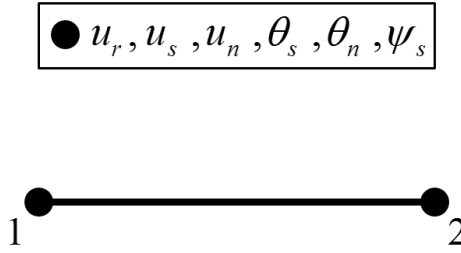


Figure 4. Constrained RZT-based beam finite element: topology and nodal degrees of freedom.

3.4 Three-node 24-dofs triangular and four-node 32-dofs quadrilateral flat shell elements

Employing the procedure adopted in the previous section to pass from the unconstrained beam element to the constrained, it is now possible to formulate a three-node 24-dofs triangular and a four-node 32-dofs quadrilateral flat shell element. As a matter of fact, the triangular and quadrilateral elements may be considered as frame

structures constituted, respectively, by three and four co-planar beams (Figure 5). The reference axes of the beams define the (x_1, x_2) plane and the shell's mid-surface. Moreover, the beams are oriented such as the positive direction of their through-the-thickness n – axis coincides with the positive direction of the z – axis, orthogonal to the (x_1, x_2) plane (the coarse drilling rotation is therefore denoted by θ_z and is equivalent to the θ_n bending rotation used for the beam case).

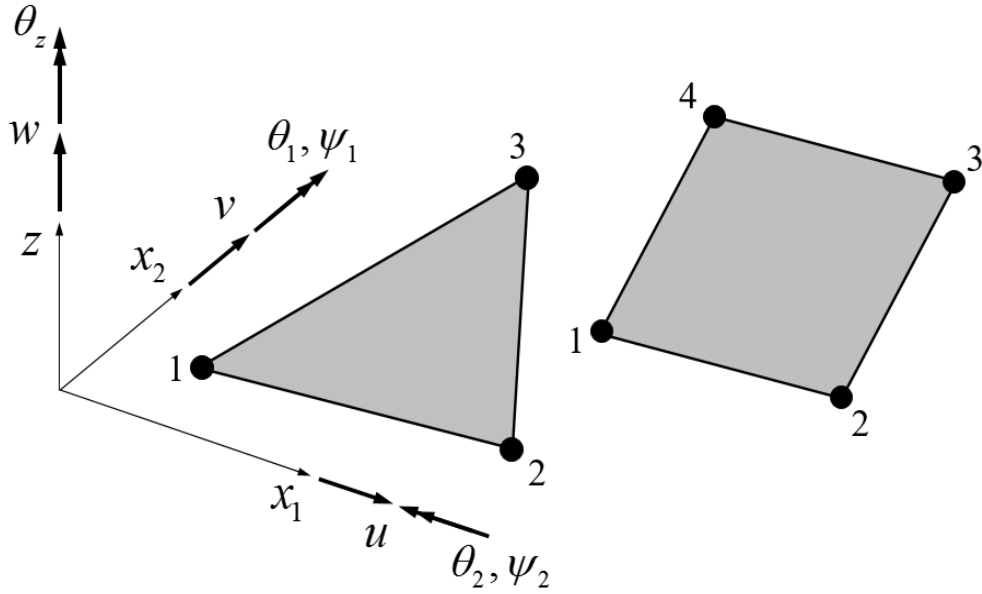


Figure 5. RZT-based flat shell elements: topology and kinematic variables.

The initial approximation for the kinematic variables is again quadratic for the displacements

$$u(x_1, x_2) = \sum_{\ell} u_{\ell} P_{\ell}(x_1, x_2) \quad v(x_1, x_2) = \sum_{\ell} v_{\ell} P_{\ell}(x_1, x_2) \quad w(x_1, x_2) = \sum_{\ell} w_{\ell} P_{\ell}(x_1, x_2) \quad (16)$$

and linear for the rotations

$$\begin{aligned}
\theta_1(x_1, x_2) &= \sum_i \theta_{1i} L_i(x_1, x_2) & \theta_2(x_1, x_2) &= \sum_i \theta_{2i} L_i(x_1, x_2) & \theta_z(x_1, x_2) &= \sum_i \theta_{zi} L_i(x_1, x_2) \\
\psi_1(x_1, x_2) &= \sum_i \psi_{1i} L_i(x_1, x_2) & \psi_2(x_1, x_2) &= \sum_i \psi_{2i} L_i(x_1, x_2)
\end{aligned} \tag{17}$$

where $i = 1, 2, \dots, n$ ranges over the n corner nodes ($n = 3$ for triangular elements, $n = 4$ for Quad elements), $\ell = 1, m_{12}, 2, m_{23}, \dots, n, m_{n1}$ ranges over the corner and the mid-edge nodes. Moreover, L_i are the area-parametric coordinates for triangular element and the isoparametric bi-linear shape functions for quadrilateral element [54]. Similarly, P_ℓ represent the quadratic shape functions for triangular element and serendipity quadratic shape functions for quadrilateral element [54] (refer also to the Appendix B).

Unconstrained shell elements are obtained (Figure 6) that are analogous to the unconstrained beam element previously discussed (Figure 3).

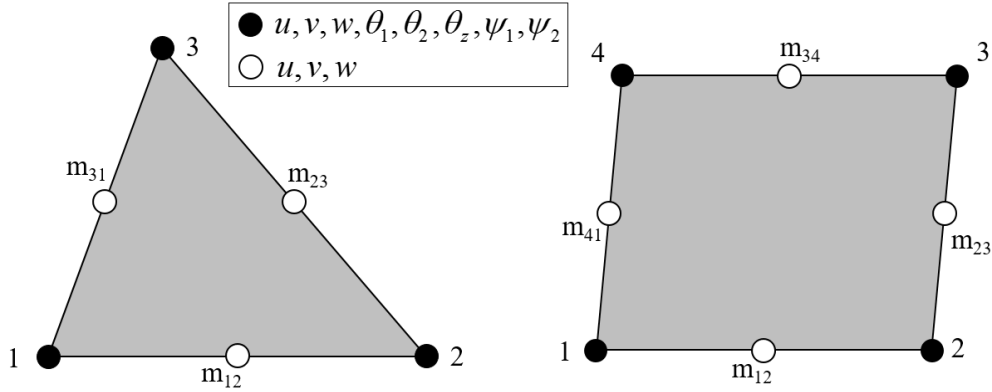


Figure 6. Unconstrained RZT-based flat shell elements: topology and nodal degrees of freedom.

Constraining conditions, Eqs. (14), are now applied to each of the 3 edges for the triangular element and to each of the 4 edges for the quadrilateral element after performing the appropriate coordinate transformation. These transformations, although straightforward, require several passages that are omitted here; the resulting expression for the plate displacements is thus given as

$$\begin{aligned}
u(x_1, x_2) &= \sum_i u_i L_i(x_1, x_2) + \sum_i \theta_{zi} Q_{2i}(x_1, x_2) \\
v(x_1, x_2) &= \sum_i v_i L_i(x_1, x_2) - \sum_i \theta_{zi} Q_{1i}(x_1, x_2) \\
w(x_1, x_2) &= \sum_i w_i L_i(x_1, x_2) + \sum_i (\theta_{1i} - \psi_{1i}) Q_{1i}(x_1, x_2) + \sum_i (\theta_{2i} - \psi_{2i}) Q_{2i}(x_1, x_2)
\end{aligned} \tag{18}$$

where Q_{1i} and Q_{2i} are particular quadratic shape functions (see Appendix B for a complete definition). Eqs. (18), and (17) can be written in the compact form

$$\bar{\mathbf{u}} = \mathbf{N} \mathbf{u}^e \tag{19}$$

with $\bar{\mathbf{u}}$ collecting the original RZT kinematic variables (\mathbf{u}) and the additional coarse drilling rotation (θ_z), $\bar{\mathbf{u}} \equiv [u \quad v \quad w \quad \theta_1 \quad \theta_2 \quad \theta_z \quad \psi_1 \quad \psi_2]^T$, and with the following definition for the matrix \mathbf{N} and the vector \mathbf{u}^e

$$\mathbf{N} \equiv \begin{bmatrix} [L_i] & \mathbf{0} & \mathbf{0} & \mathbf{0} & \mathbf{0} & [Q_{2i}] & \mathbf{0} & \mathbf{0} \\ \mathbf{0} & [L_i] & \mathbf{0} & \mathbf{0} & \mathbf{0} & -[Q_{1i}] & \mathbf{0} & \mathbf{0} \\ \mathbf{0} & \mathbf{0} & [L_i] & [Q_{1i}] & [Q_{2i}] & \mathbf{0} & -[Q_{1i}] & -[Q_{2i}] \\ \mathbf{0} & \mathbf{0} & \mathbf{0} & [L_i] & \mathbf{0} & \mathbf{0} & \mathbf{0} & \mathbf{0} \\ \mathbf{0} & \mathbf{0} & \mathbf{0} & \mathbf{0} & [L_i] & \mathbf{0} & \mathbf{0} & \mathbf{0} \\ \mathbf{0} & \mathbf{0} & \mathbf{0} & \mathbf{0} & \mathbf{0} & [L_i] & \mathbf{0} & \mathbf{0} \\ \mathbf{0} & \mathbf{0} & \mathbf{0} & \mathbf{0} & \mathbf{0} & \mathbf{0} & [L_i] & \mathbf{0} \\ \mathbf{0} & \mathbf{0} & \mathbf{0} & \mathbf{0} & \mathbf{0} & \mathbf{0} & \mathbf{0} & [L_i] \end{bmatrix} \tag{20}$$

$$\mathbf{u}^e \equiv [[u_i] \quad [v_i] \quad [w_i] \quad [\theta_{1i}] \quad [\theta_{2i}] \quad [\theta_{zi}] \quad [\psi_{1i}] \quad [\psi_{2i}]]^T \tag{21}$$

The resulting constrained shell elements (analogous to the beam constrained element of Figure 4) have eight nodal degrees of freedom defined on each corner node: three displacements u , v and w (directed along the x_1 -, x_2 - and z -axis, respectively), two bending rotations θ_1 and θ_2 (around the x_2 - and x_1 -axis,

respectively), the coarse drilling rotation θ_z , and two zigzag rotations ψ_1 and ψ_2 (around the x_2 – and x_1 – axis, respectively) (Figure 7).

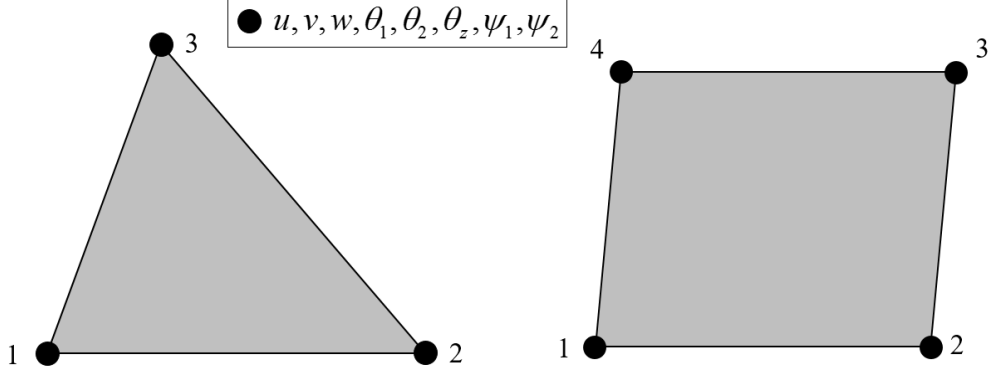


Figure 7. Constrained RZT-based flat shell elements: topology and nodal degrees of freedom.

3.5 Element mass and stiffness matrix and nodal load vector

Substituting Eq. (19) into the definition of the strain measures (Appendix A) yields

$$\begin{aligned} \mathbf{e}_m &\equiv \mathbf{B}_m \mathbf{u}^e \\ \mathbf{e}_b &\equiv \mathbf{B}_b \mathbf{u}^e \\ \mathbf{e}_s &\equiv \mathbf{B}_s \mathbf{u}^e \end{aligned} \quad (22)$$

where \mathbf{B}_m , \mathbf{B}_b and \mathbf{B}_s are, respectively, the membrane, bending and transverse shear strain-displacement matrices which contain the derivatives of the shape functions with respect to the in-plane coordinates x_1 and x_2 .

Introducing the finite element approximation (Eqs. (19) and (22)) into the variational statement Eq. (5)

$$\delta \mathbf{u}^{e^T} (\mathbf{M}^e \ddot{\mathbf{u}}^e + \mathbf{K}^e \mathbf{u}^e - \mathbf{f}^e) = 0 \quad (23)$$

Eq. (23) yields the equation of motion of the finite element in its local coordinate system (x_1, x_2, z)

$$\mathbf{M}^e \ddot{\mathbf{u}}^e + \mathbf{K}^e \mathbf{u}^e - \mathbf{f}^e = \mathbf{0} \quad (24)$$

where:

- \mathbf{M}^e is the element mass matrix of the element

$$\mathbf{M}^e \equiv \int_S \tilde{\mathbf{N}}^T \Gamma \tilde{\mathbf{N}} dS \quad (25)$$

where $\tilde{\mathbf{N}}$ is obtained from matrix \mathbf{N} (Eq. (20)) by removing its sixth row.

- \mathbf{K}^e denotes the stiffness matrix of the element and is given by the sum of the membrane, bending, coupling, and transverse shear contributions, defined as follows

$$\begin{aligned} \mathbf{K}_m^e &\equiv \int_S \mathbf{B}_m^T \mathbf{A} \mathbf{B}_m dS \\ \mathbf{K}_b^e &\equiv \int_S \mathbf{B}_b^T \mathbf{D} \mathbf{B}_b dS \\ \mathbf{K}_c^e &\equiv \int_S (\mathbf{B}_m^T \mathbf{B} \mathbf{B}_b + \mathbf{B}_b^T \mathbf{B}^T \mathbf{B}_m) dS \\ \mathbf{K}_s^e &\equiv \int_S \mathbf{B}_s^T \mathbf{G} \mathbf{B}_s dS \end{aligned} \quad (26)$$

- \mathbf{f}^e is the nodal forces vector of the element.

3.6 Stabilization

The procedure discussed in Sections 3.1 to 3.4 does not bring into the formulation of the triangular and quadrilateral elements a dependence on the “drilling” component of the zigzag rotation, ψ_z . In order to model built-up or curved shell structures, it is necessary to connect elements that are not co-planar. As a consequence, the ψ_z nodal

degree of freedom has to be introduced and the vector of nodal degrees of freedom is expanded

$$\mathbf{q}^e \equiv \begin{bmatrix} [u_i] & [v_i] & [w_i] & [\theta_i] & [\theta_{2i}] & [\theta_{zi}] & [\psi_{1i}] & [\psi_{2i}] & [\psi_{zi}] \end{bmatrix}^T \quad (27)$$

The mass matrix and stiffness matrix (Eqs. (25) and (26)) as well as the force vector are correspondingly expanded with zero coefficients, thus obtaining $\tilde{\mathbf{M}}^e$, $\tilde{\mathbf{K}}^e$ and $\tilde{\mathbf{f}}^e$. Analogously to the interpolation used for the rotational degrees of freedom, linear shape functions are used for the approximation of ψ_z

$$\psi_z(x_1, x_2) = \sum_i \psi_{zi} L_i(x_1, x_2) = [L_i(x_1, x_2)] \{\psi_{zi}\} \quad (28)$$

Following one of the approaches proposed in [54] where a penalty formulation was employed to account for the coarse drilling rotation θ_z within FSDT-based shell finite elements, the artificial stiffness coefficients corresponding to ψ_z are introduced by means of an additional penalty term. Accordingly, the total potential energy of each element, Π , becomes

$$\Pi^* \equiv \Pi + \lambda_\psi \frac{C_\psi}{2} \int_S (\psi_z(x_1, x_2) - \bar{\psi}_z)^2 dS \quad (29)$$

where λ_ψ is a penalty parameter, C_ψ is a constant (units of force per unit length) introduced for dimensional consistency and $\bar{\psi}_z$ is the element-level average value for ψ_z

$$\bar{\psi}_z \equiv \frac{1}{S} \int_S \psi_z(x_1, x_2) dS \quad (30)$$

By introducing Eq. (28) into Eq. (30), we obtain

$$\begin{aligned} \bar{\psi}_z &= \frac{1}{S} \int_S [L_i(x_1, x_2)] \{\psi_{zi}\} dS \\ &= \frac{1}{S} \int_S [L_i(x_1, x_2)] dS \{\psi_{zi}\} \\ &= [a_i] \{\psi_{zi}\} \end{aligned} \quad (31)$$

Eq. (29) can now be rewritten by using Eqs. (28) and (31)

$$\Pi^* = \Pi + \frac{1}{2} \{\psi_{zi}\}^T \lambda_\psi C_\psi [K_\psi] \{\psi_{zi}\} \quad (32)$$

where

$$[K_\psi] \equiv \int_S \left([L_i(x_1, x_2)]^T [L_i(x_1, x_2)] - [a_i]^T [a_i] \right) dS \quad (33)$$

Following [70], a suitable choice for the penalty parameter λ_ψ is 10^{-5} . Moreover, owing to the fact that the stiffness being represented by the matrix defined in Eq. (33) is related to the drilling zigzag rotation, the dimensional coefficient is calculated as

$$C_\psi \equiv \sqrt{G_{22}^2 + G_{44}^2} \quad (34)$$

where G_{22} and G_{44} are defined in Appendix A. Refer also to Appendix C for further details on matrix $[K_\psi]$ for triangular elements.

The matrix $\lambda_\psi C_\psi [K_\psi]$ is expanded ($\lambda_\psi C_\psi \mathbf{K}_\psi^e$) and summed to the element stiffness matrix

$$\tilde{\mathbf{K}}^e + \lambda_\psi C_\psi \mathbf{K}_\psi^e \quad (35)$$

As demonstrated by Tessler [67,68], after applying the interdependent interpolation scheme to the in-plane displacements, the Allman shape functions can be obtained [63,64]. The Allman-type shape functions, besides providing a drilling-degree-of-freedom formulation, introduce into the finite element zero-energy modes [54,58-60,71]. When all the coarse drilling rotations θ_z assume the same value, the deformation energy associated to this rotation is zero and a spurious mode arises. Zero energy modes have to be eliminated in order to guarantee the convergence of the finite element.

According to Allman [63], this goal may be achieved by assigning a constant value to at least one drilling rotation of the model; this numerical expedient allows the stiffness matrix to become positive definite thus improving the convergence properties of the method. Although effective, this technique is highly unfit for large scale models.

Hughes and Brezzi [59] proposed a method that allows to remove the spurious modes by modifying the energy functional and penalizing the zero-energy modes. This strategy has been used for the development of several membrane finite elements [60,72] and has been extended to cope with curved shells as well [71].

When the interdependent interpolation strategy is used to formulate a finite element with parabolic displacements, it is also possible to inhibit the spurious modes by employing a stabilization matrix based on the finite element's *edge reinforcement* proposed by Tessler [70]. The energy functional is modified by introducing a term that penalizes the zero-energy modes, similarly to the Brezzi and Hughes's approach [59], and is derived enforcing, in a weak sense, the Kirchhoff constraints for slender beams. These slender beams are superimposed to the element's edges thus providing a local 1D

reinforcement. Recalling the beam-frame representation (Figure 2), it can be observed that for a very thin beam the Kirchhoff condition holds: the in-plane shear strain evaluated at the midpoint is imposed to be zero thus yielding (refer to definition in Eq. (7))

$$(\gamma_{rs})_m \equiv (\gamma_{rs})_{r=L/2} = (-\theta_n + u_{s,r})_{r=L/2} = -\frac{1}{2}(\theta_{n1} + \theta_{n2}) + \frac{1}{L}(u_{s2} - u_{s1}) = 0 \quad (36)$$

Considering the beam to be superimposed to the edge of the triangular or quadrilateral element between nodes i and j , using the θ_z notation for the coarse drilling rotation and by means of the appropriate coordinate transformation, Eq. (36) is modified as follows

$$(\gamma_{rs})_{m_{ij}} = \frac{1}{\ell_{ij}^2}((x_{1j} - x_{1i})(v_j - v_i) - (x_{2j} - x_{2i})(u_j - u_i)) - \frac{1}{2}(\theta_{zi} + \theta_{zj}) = 0 \quad (37)$$

where ℓ_{ij} is the length of the edge between nodes i and j , (x_{1i}, x_{2i}) are the local in-plane coordinates of the node i , the indices i and j follow the usual cyclic permutation ($i = 1, 2, 3$ and $j = 2, 3, 1$ for the triangular element, $i = 1, 2, 3, 4$ and $j = 2, 3, 4, 1$ for the quadrilateral element). Eq. (37) can be written in matrix form by expressing $(\gamma_{rs})_{m_{ij}}$ in terms of the nodal degrees of freedom

$$(\gamma_{rs})_{m_{ij}} = (\mathbf{B}_\gamma^e)_{ij} \mathbf{q}^e = 0 \quad (38)$$

Eq. (38) can be enforced at the element level by considering the sum of the contributions coming from the edges

$$\sum (\gamma_{rs})_{m_{ij}}^2 = \mathbf{q}^{e^T} \left(\sum (\mathbf{B}_\gamma^e)_{ij}^T (\mathbf{B}_\gamma^e)_{ij} \right) \mathbf{q}^e = \mathbf{q}^{e^T} \mathbf{K}_\theta^e \mathbf{q}^e = 0 \quad (39)$$

The spurious modes are hence suppressed by way of a penalty formulation that enforces weakly the condition derived from Eq. (39), i.e., by further updating the element stiffness matrix as follows

$$\tilde{\mathbf{K}}^e + \lambda_\psi C_\psi \mathbf{K}_\psi^e + \lambda_\theta C_\theta \mathbf{K}_\theta^e \quad (40)$$

where λ_θ is a penalty parameter set to 10^{-5} and C_θ is a constant (units of Joule) introduced for dimensional consistency and set to be

$$C_\theta \equiv S \sqrt{G_{11}^2 + G_{33}^2} \quad (41)$$

with G_{11} and G_{33} defined in Appendix A.

4. NUMERICAL RESULTS

The first set of numerical results is related to the linear bending of a flat multilayered structure and aims at showing the convergence properties of the proposed elements with respect to the analytic RZT solution. The same example problem is used to investigate the elements' performance when distorted meshes are used and to verify that the shear-locking problem is eliminated for a realistic range of edge length-to-thickness ratios.

In the second part of this section, a hemispherical sandwich structure is considered to assess the RZT-based elements for the linear static response and the modal analysis of doubly-curved multilayered shells.

4.1. Convergence, distorted mesh effect and shear-locking

In order to investigate the convergence properties, the effect of distorted and irregular meshes and the absence of shear-locking for the proposed RZT-based shell elements, an analytic RZT solution should be available as reference result. This solution exists in the Navier's form for simply supported rectangular plates subjected to a bi-sinusoidal transverse load [31].

A square plate is considered with edge length a and thickness $2h$. The plate is simply supported on all the edges and subjected to a bi-sinusoidal transverse load with maximum amplitude q_0 . Table 1 shows the stacking sequence and Table 2 reports the material properties of the plate.

Table 1. Stacking sequence of the simply supported square plate (layer sequence is in the positive z -direction).

Thicknesses ($h^{(k)}/h$)	Materials	Orientations (degrees)
$[\frac{1}{30} / \frac{1}{30} / \frac{1}{30} / \frac{21}{30} / \frac{2}{30} / \frac{2}{30} / \frac{2}{30}]$	$[C / C / C / R / C / C / C]$	$[0 / 90 / 0 / 0 / 0 / 90 / 0]$

Table 2. Materials' mechanical properties.

Material code	E_1 (MPa)	E_2 (MPa)	E_3 (MPa)	ν_{12}	ν_{13}	ν_{23}	G_{12} (MPa)	G_{13} (MPa)	G_{23} (MPa)
C (Carbon-Epoxy UD)	110000	7857	7857	0.33	0.33	0.49	3292	3292	1292
R (Rohacell® foam)	40.3			0.3			12.4		

The plate is a non symmetric sandwich with multilayered composite facesheets and a foam core. Table 3 reports the exact non-dimensional maximum deflection of the plate according to RZT for different $a/2h$ ratios.

Table 3. Exact non-dimensional maximum deflection of the square plate according to RZT,

$\tilde{w}_{RZT} \equiv \max(w_{RZT}) \cdot (D_{11}/q_0 a^4)$, where D_{11} is the bending stiffness of the plate along the x_1 direction.

$a/2h$	10^1	$5 \cdot 10^1$	10^2	$5 \cdot 10^2$	10^3	$5 \cdot 10^3$	10^4	$5 \cdot 10^4$	10^5	$5 \cdot 10^5$	10^6
$1000 \tilde{w}_{RZT}$	119.8	12.63	7.890	6.303	6.253	6.237	6.237	6.237	6.237	6.237	6.236

At first, the convergence of the proposed FEM solution to the exact RZT deflection is investigated for a moderately thick case, $a/2h = 10$, and when using regular mesh patterns. The symmetry of the problem is taken into account and $1/4$ of the plate is discretized according to the schemes represented in Figure 8.

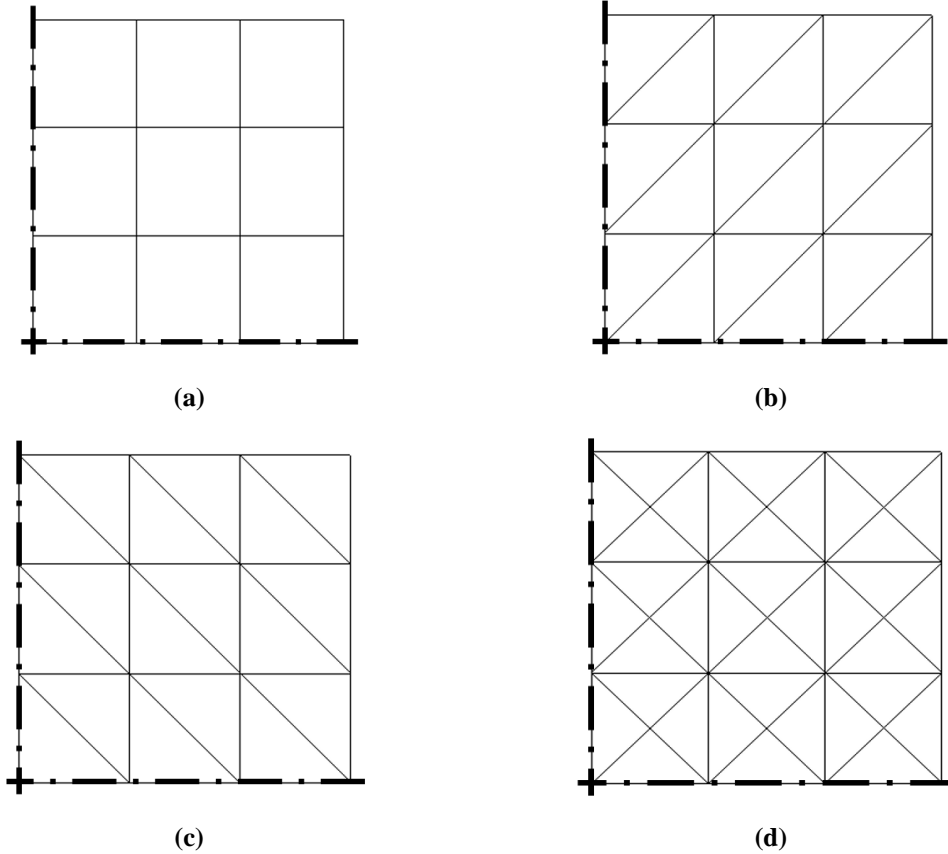


Figure 8. Regular mesh schemes for $1/4$ of the square plate characterized by N_e = number of subdivisions per edge and N_n = total number of nodes: (a) Quad mesh ($N_e = 3$, $N_n = 16$), (b) Tria(1) mesh ($N_e = 3$, $N_n = 16$), (c) Tria(2) mesh ($N_e = 3$, $N_n = 16$), (d) Tria(3) mesh ($N_e = 3$, $N_n = 25$).

Figure 9 shows the percent error of the RZT FEM maximum deflection with respect the RZT exact one, $E\%(w)$, as a function of the number of nodes, N_n , for the considered regular mesh schemes.

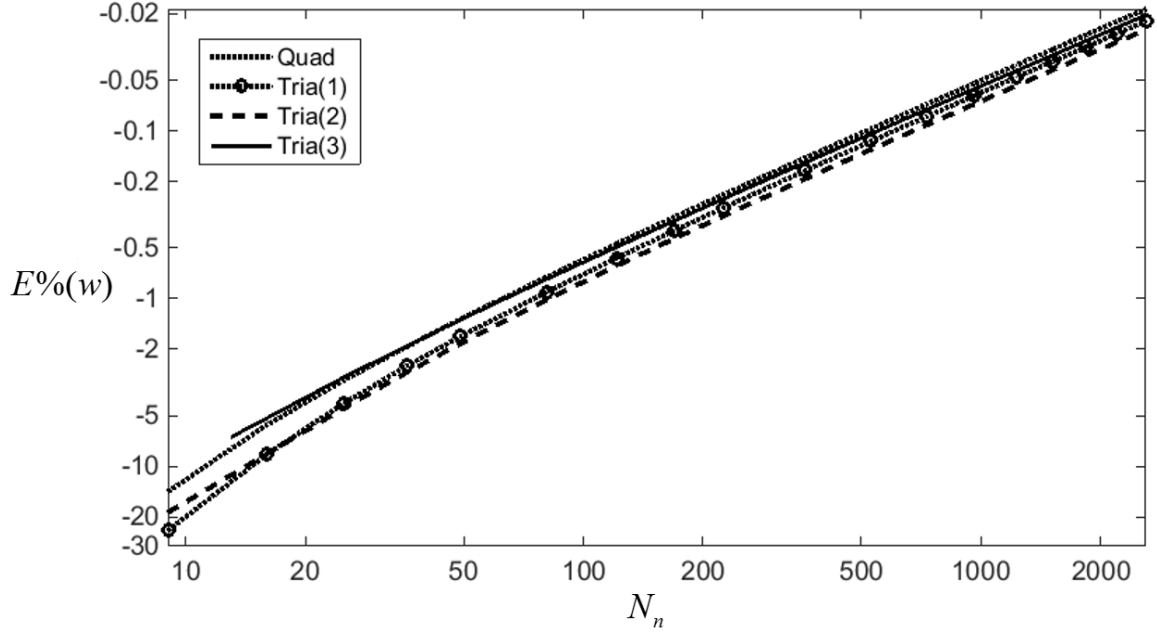


Figure 9. Square plate problem: convergence of the RZT FEM maximum deflection to the RZT exact one for regular mesh patterns.

When the number of nodes is at least 100, all of the regular mesh patters show similar performances and guarantee that the maximum deflection is evaluated with an error that is lower than 1%. For coarser mesh schemes, the use of Quad elements or Tria elements arranged according to the pattern (3) (Figure 8), provides slightly more accurate predictions.

The effect of using irregular and distorted mesh patters has also been investigated. Figure 10 shows the considered irregular discretization schemes and reports the corresponding number of nodes.

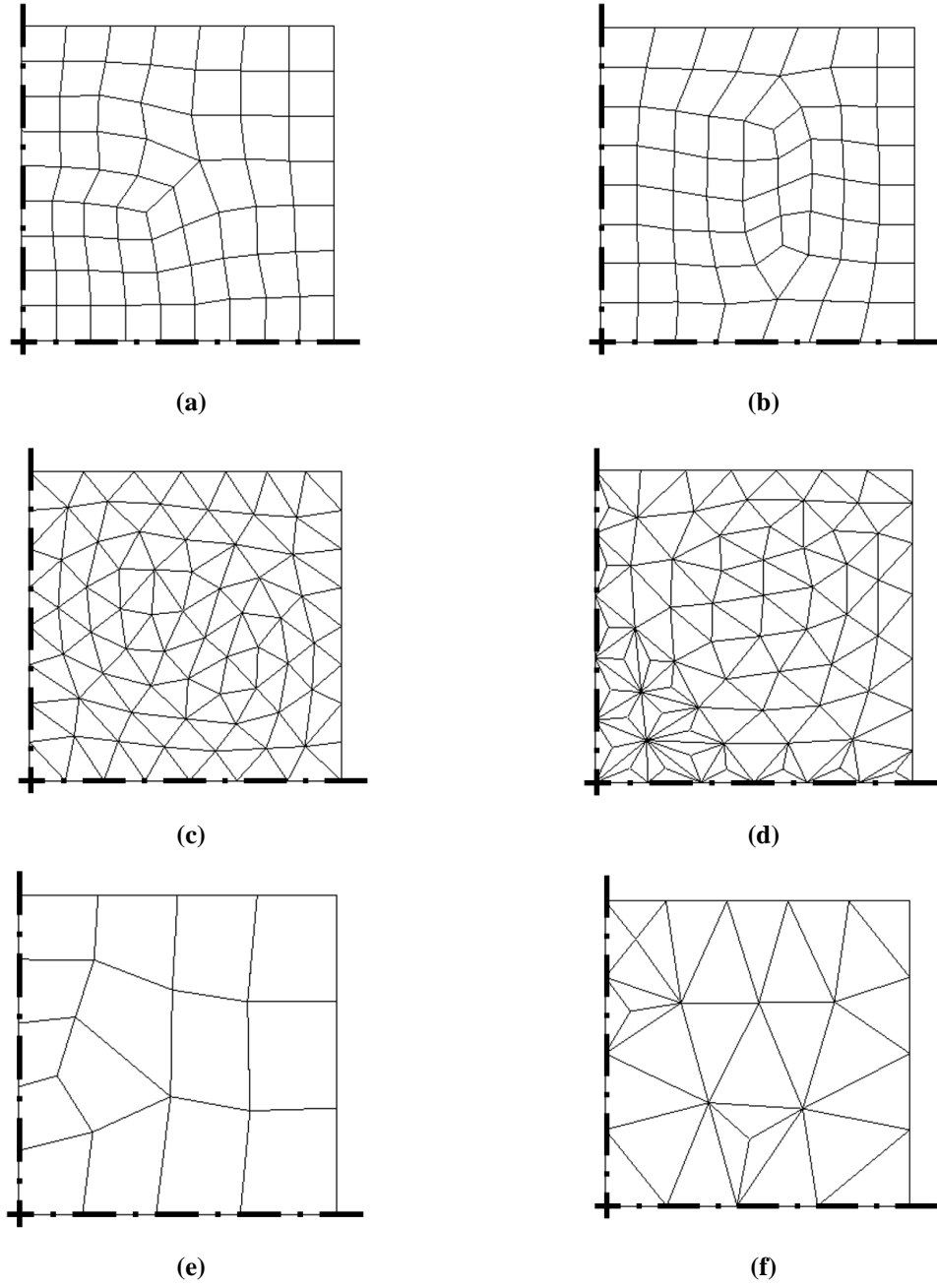


Figure 10. Irregular mesh schemes for $\frac{1}{4}$ of the square plate: (a) mesh D1 ($N_n = 82$), (b) mesh D2 ($N_n = 82$), (c) mesh D3 ($N_n = 81$), (d) mesh D4 ($N_n = 82$), (e) mesh D5 ($N_n = 24$), (f) mesh D6 ($N_n = 25$).

Figure 11 allows to compare the performances of the regular and irregular mesh schemes being considered.

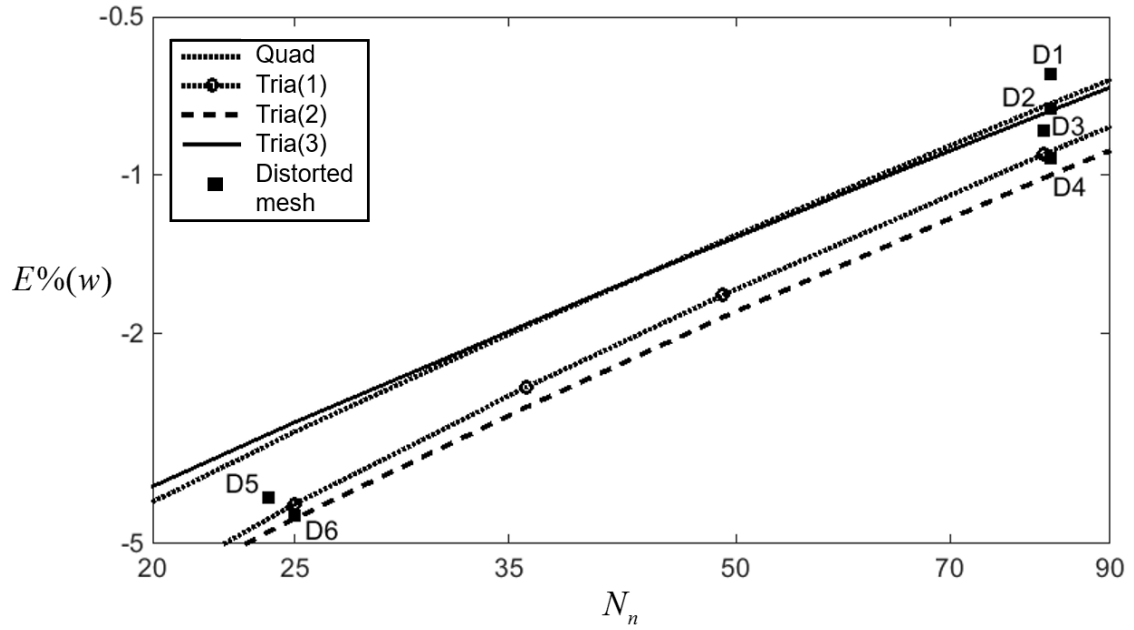


Figure 11. Square plate problem: comparison between the performances of the irregular and regular mesh schemes.

When the discretization is based on an adequate number of elements and nodes (irregular mesh schemes D1–D4, $N_n = 81, 82$), the percent errors on the maximum deflection are very similar to those obtained with regular mesh patterns (scheme D1 is slightly better than the best regular scheme due to a smooth transition between smaller elements – where higher strain gradients are present – and bigger elements). For coarser irregular meshes (schemes D5, D6, $N_n = 24, 25$), the performances are comparable to those of the less accurate regular discretizations. These results demonstrate that the proposed shell elements based on RZT are adequately robust with respect to the mesh irregularity.

A further investigation has been performed to verify if the interdependent interpolation strategy adopted to develop the proposed shell elements is able to eliminate the shear locking phenomenon. The same square plate problem is considered with $a/2h$ ratio ranging from 10 to 10^6 . The exact RZT maximum deflection for the different cases is reported in Table 3. The RZT FEM results are obtained with regular

mesh patterns (Figure 8) and a number of elements and nodes that guarantee convergence ($N_e = 50$ and $N_n = 2601$ for mesh patterns Quad, Tria(1) and Tria(2), $N_e = 35$ and $N_n = 2521$ for mesh pattern Tria(3)). Figure 12 shows the ratio of the FEM to the exact RZT maximum deflection as a function of the $a/2h$ ratio.

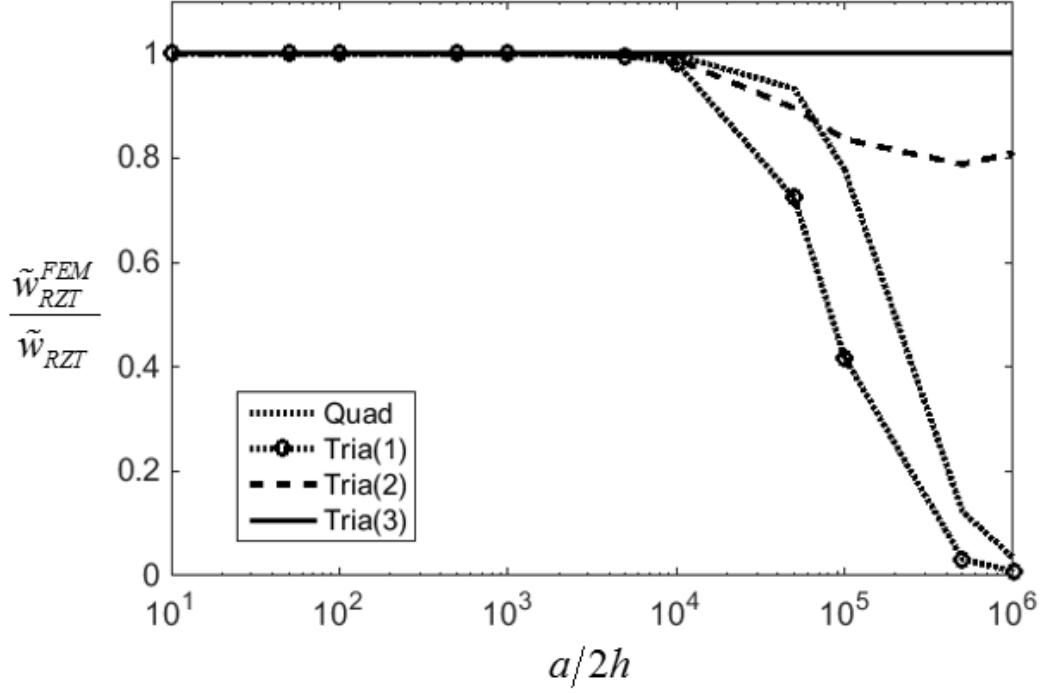


Figure 12. Square plate problem: performance of the RZT-shell finite elements for thinner and thinner plates.

All of the FEM solutions are accurate within a range of realistic edge length-to-thickness ratios (from 10 to 10^4). In particular, up to $a/2h = 10^3$, the FEM deflections are in excellent agreement with the exact deflections. When reaching $a/2h = 10^4$, some mesh patterns lead to errors that do not exceed 2%. For thinner plates, shear locking occurs with different levels of severity for the different mesh schemes. The Tria(3) mesh solution is the only one able to provide accurate response predictions also for extremely thin plates.

4.2. Doubly-curved sandwich structure

A benchmark problem similar to the pinched cap described in [73] is considered, with changes in the material lay-up (in order to introduce the zigzag effect in the structural response) and boundary conditions. A hemispherical cap with mean radius $R = 10\text{ m}$ and a 12° hole cutout on the top is considered (Figure 13). Symmetry of the problem is taken into account and $\frac{1}{4}$ of the structure is analyzed.

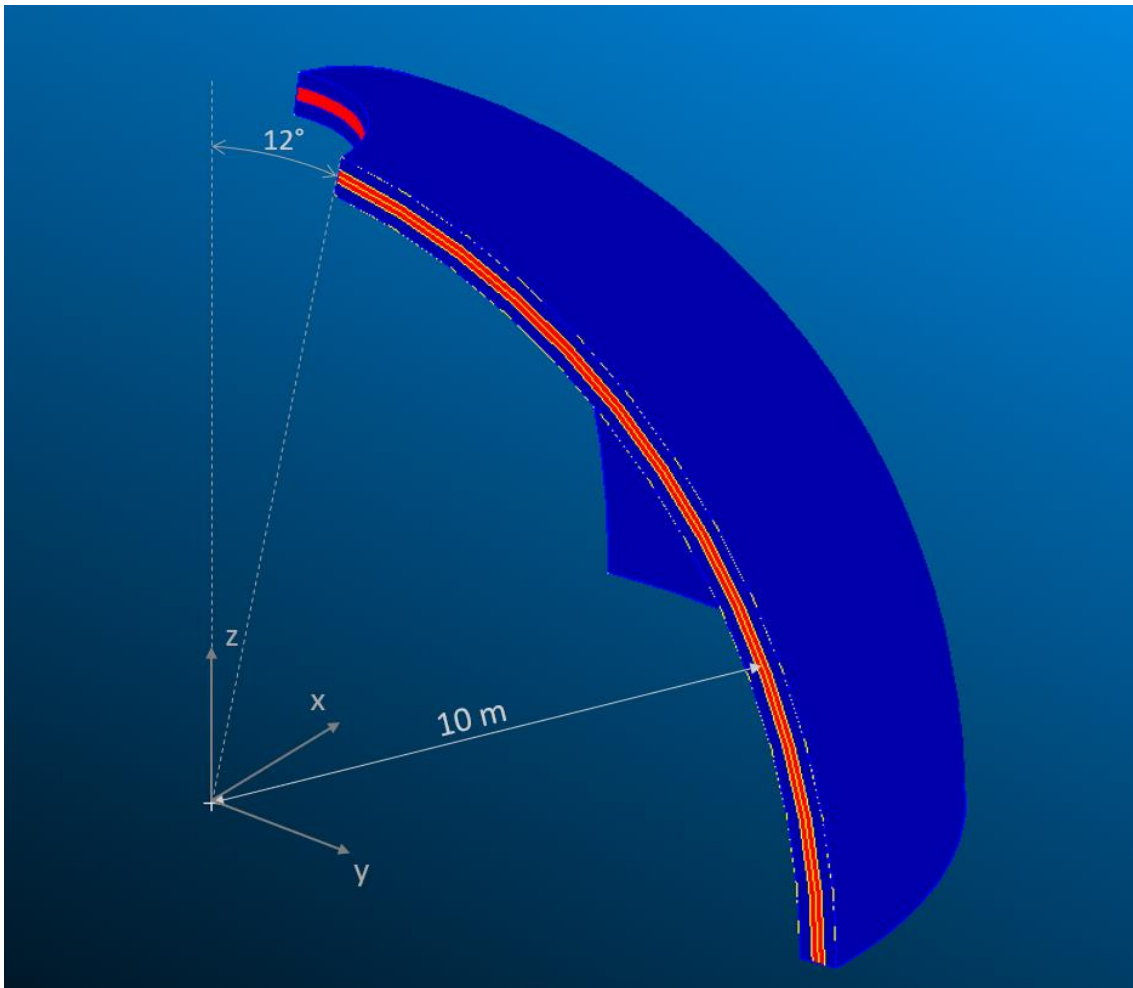


Figure 13. Pinched cap geometry ($\frac{1}{4}$ of the structure is represented).

The structure has a sandwich-like stacking sequence (Table 4) with thick Aluminum facesheets and a weak and lightweight core (Table 5).

Table 4. Pinched cap stacking sequence.

Thickness (m)	Material
[0.2 / 0.2 / 0.2]	[A / C / A]

Table 5. Materials' mechanical properties.

Material	E (MPa)	ν	ρ (Kg/m ³)
A	73000	0.33	2800
C	73	0.33	2.80

A high-fidelity 3D model of the structure has been obtained using MSC/Nastran. The model is made up of 60000 HEXA8 elements, 100 along each edge of the structure and 6 along the thickness, for a total of 180000 nodal degrees of freedom (Figure 14).

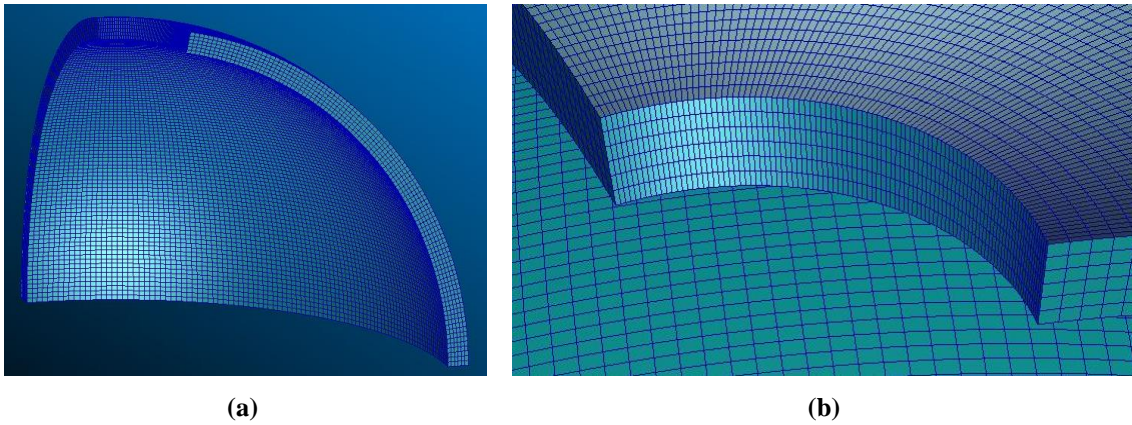


Figure 14. MSC/NASTRAN 3D model of the pinched cap: (a) overview, (b) zoomed view around the hole cutout.

The RZT shell model is obtained using regular mesh patterns, with 8, 16, 32, 64 subdivisions on each side (Figure 15).

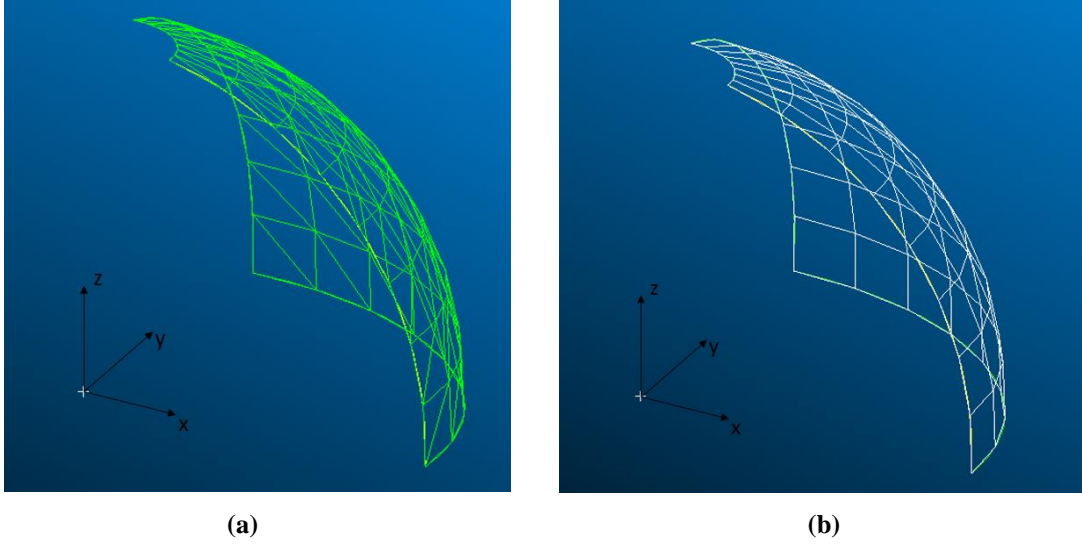


Figure 15. RZT shell model of the pinched cap with 8 x 8 subdivisions and regular mesh schemes: (a) triangular mesh (128 elements), (b) quadrilateral mesh (64 elements).

For comparison purposes, a shell FE model based on 64 x 64 subdivisions and FSDT-based flat shell elements is also considered. Both triangular (Tria) and quadrilateral (Quad) FSDT elements have been implemented following the same formulation presented for the RZT elements. Moreover, a transverse-shear strain-energy based consistent shear correction factor has been applied according to the procedure proposed in [8]. Table 6 summarizes the properties of the shell and 3D FE models considered.

Table 6. Properties of the FE models used for the static and modal analysis of the pinched cap.

	FSDT Quad (Tria)	RZT Quad (Tria)				MSC/NASTRAN HEXA8
Number of subdivisions along the edges	64	8	16	32	64	100
Number of subdivisions along the thickness	1	1	1	1	1	6
Number of elements	4096 (8192)	64 (128)	256 (512)	1024 (2048)	4096 (8192)	60000
Number of dofs	25350	729	2601	9801	38025	180000

The structure is loaded by alternating pinching loads with magnitude $F = 1000 \text{ N}$, acting along the radial direction and applied in points p1 and p2 (Figure 16(a)).

Symmetry boundary conditions are applied on the two meridian edges. Figure 16(b) shows that the loads are equally divided among the two facesheets of the MSC/NASTRAN 3D model in order to avoid thickness-stretching effects that are not taken into account in the current RZT formulation.

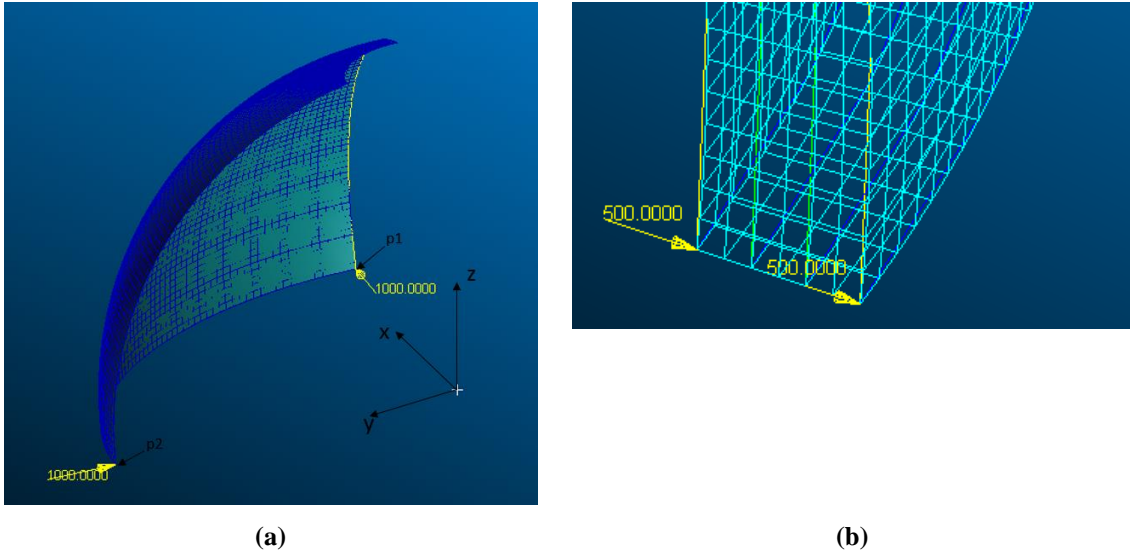


Figure 16. Pinched cap static problem: (a) RZT regular Quad shell model (64 x 64) with applied loads, (b) MSC/NASTRAN 3D model with applied loads.

The reference solution is represented by the x - and z -mean displacements of the 7 nodes of the 3D mesh that correspond to the point p1 on the 2D mesh: $U_x = 9.151\text{E-}05$, $U_z = 4.249\text{E-}05$. Tables 7 and 8 report the percent errors of the FSDT and RZT shell models with respect to the reference solution.

Table 7. Pinched cap static response: percent errors of the FSDT and RZT triangular shell models with respect to the MSC/NASTRAN 3D reference solution.

	FSDT Tria	RZT Tria			
Number of subdivisions along the edges	64	8	16	32	64
$E\%(U_x)$	96.72%	-11.32%	-3.92%	-1.52%	-0.52%
$E\%(U_z)$	25.37%	-5.67%	-1.91%	-0.93%	-0.47%

Table 8. Pinched cap static response: percent errors of the FSDT and RZT quadrilateral shell models with respect to the MSC/NASTRAN 3D reference solution.

	FSDT Quad	RZT Quad			
Number of subdivisions along the edges	64	8	16	32	64
$E\%(U_x)$	111.09%	-7.13%	-2.09%	-0.65%	-0.07%
$E\%(U_z)$	26.02%	-2.11%	-0.75%	-0.39%	-0.13%

Results show a rapid convergence to the reference results for the RZT-based elements, in particular for the Quad elements that exhibit errors lower than 1% for a 32 x 32 mesh. The FSDT-based shell model leads to unacceptable errors even adopting a consistent shear correction factor and a refined mesh. This is due to the poor description of the through-the-thickness normal distortion (zigzag effect) that plays a key role in the structural deformation of the considered sandwich pinched cap.

The same structure is now assumed to be clamped along the base edge and the first ten vibration frequencies are evaluated. The MSC/NASTRAN reference results are reported in Table 9 and Tables 10 and 11 show the performances of the FSDT and RZT shell models.

Table 9. Pinched cap natural frequencies obtained with the MSC/NASTRAN 3D model.

Mode order	1	2	3	4	5	6	7	8	9	10
Natural frequency (Hz)	6.55	8.40	18.72	19.82	32.93	33.87	47.38	51.03	66.56	71.12

Table 10. Pinched cap natural frequencies: percent errors of the FSDT and RZT triangular shell models with respect to the MSC/NASTRAN 3D reference solution.

	FSDT Tria	RZT Tria			
Number of subdivisions along the edges	64	8	16	32	64
E%(ω_1)	-17.48%	12.91%	2.78%	1.00%	0.60%
E%(ω_2)	-17.52%	10.70%	2.60%	0.60%	0.13%
E%(ω_3)	-27.21%	14.14%	2.82%	0.67%	0.20%
E%(ω_4)	-25.61%	11.12%	2.50%	0.74%	0.29%
E%(ω_5)	-35.85%	11.77%	2.99%	0.79%	0.26%
E%(ω_6)	-36.20%	20.32%	3.69%	0.95%	0.31%
E%(ω_7)	-42.94%	19.34%	4.19%	1.06%	0.35%
E%(ω_8)	-44.69%	29.39%	5.35%	1.29%	0.42%
E%(ω_9)	-50.21%	18.43%	5.66%	1.41%	0.47%
E%(ω_{10})	-51.56%	19.26%	5.88%	1.47%	0.48%

Table 11. Pinched cap natural frequencies: percent errors of the FSDT and RZT quadrilateral shell models with respect to the MSC/NASTRAN 3D reference solution.

	FSDT Quad	RZT Quad			
Number of subdivisions along the edges	64	8	16	32	64
E%(ω_1)	-17.64%	7.01%	1.71%	0.76%	0.52%
E%(ω_2)	-17.66%	5.52%	1.25%	0.28%	0.03%
E%(ω_3)	-27.40%	7.01%	1.36%	0.35%	0.10%
E%(ω_4)	-25.79%	4.86%	1.13%	0.36%	0.15%
E%(ω_5)	-36.08%	5.41%	1.25%	0.36%	0.13%
E%(ω_6)	-36.43%	8.92%	1.53%	0.37%	0.09%
E%(ω_7)	-43.21%	9.45%	1.75%	0.48%	0.16%
E%(ω_8)	-44.94%	14.54%	2.34%	0.52%	0.13%
E%(ω_9)	-50.51%	12.86%	2.82%	0.76%	0.26%
E%(ω_{10})	-51.83%	13.73%	2.96%	0.69%	0.20%

A 32 x 32 mesh with quadrilateral RZT shell elements is able to guarantee errors lower than 1% over the first ten natural frequencies. Using triangular RZT shell elements, the same accuracy is obtained for the first 6 frequencies. Once again, FSDT shell models provides poor response predictions with a 64 x 64 mesh.

The effect of using irregular mesh patterns has also been investigated. Figure 17 shows the triangular, quadrilateral and mixed mesh schemes that have been considered for this study.

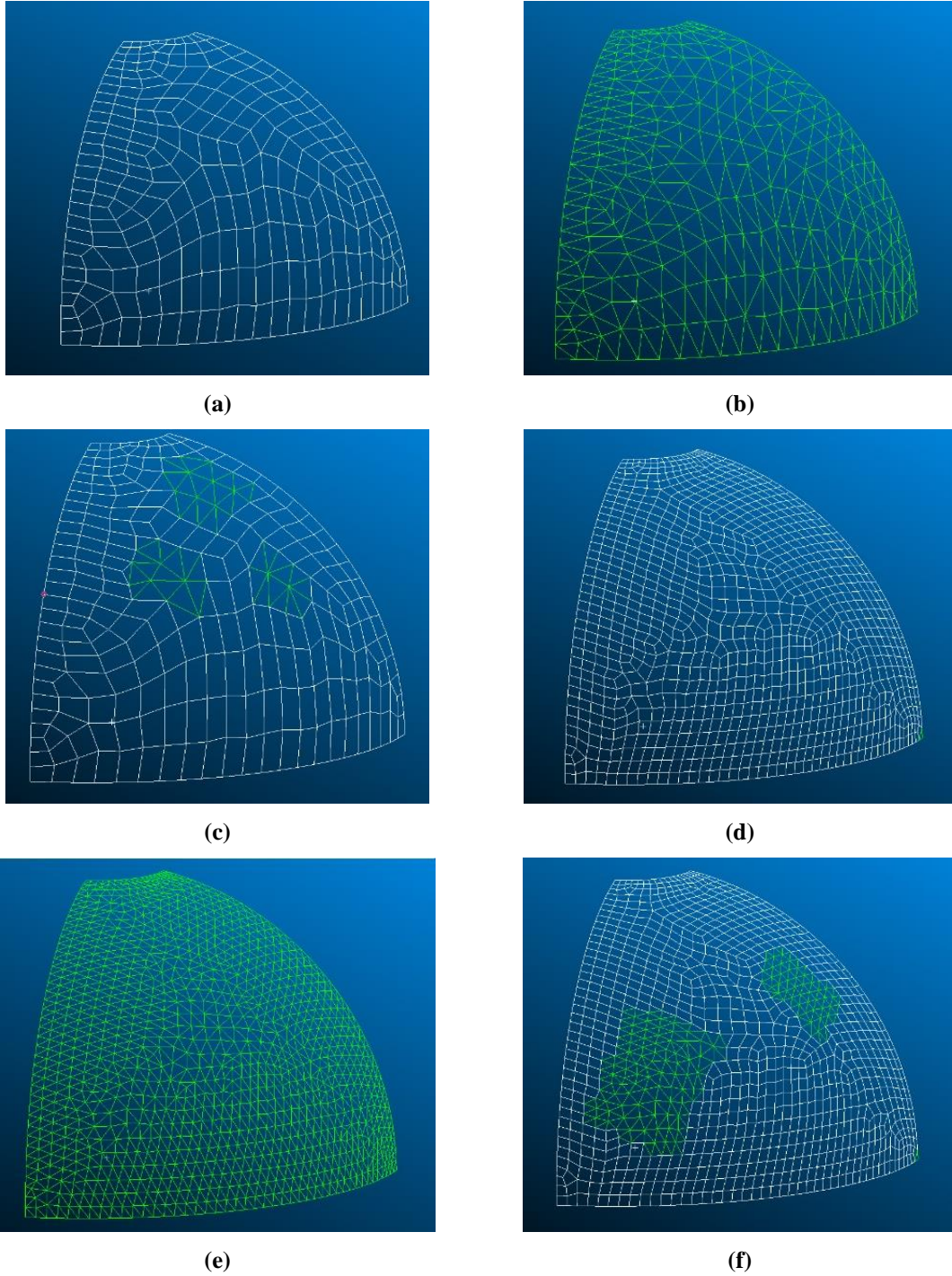


Figure 17. Irregular mesh schemes for the pinched cap: (a) mesh Q1 ($N_n = 283$), (b) mesh T1 ($N_n = 283$), (c) mesh QT1 ($N_n = 283$), (d) mesh Q2 ($N_n = 1087$), (e) mesh T2 ($N_n = 1087$), (f) mesh QT2 ($N_n = 1087$).

Coarse mesh patterns Q1, T1 and QT1 have 283 nodes and can be compared to regular mesh schemes with 16 x 16 subdivisions (289 nodes). Similarly, mesh patterns Q2, T2 and QT2 have 1087 nodes thus being comparable to 32 x 32 regular meshes (1089 nodes). Table 12 compares the accuracy of the RZT shell model with irregular mesh schemes (Q1, T1 and QT1) and regular mesh schemes (16 x 16) for the first 5 natural frequencies. Table 13 reports the same results for more refined meshes, irregular (Q2, T2 and QT2) and regular (32 x 32).

Table 12. Pinched cap natural frequencies: percent errors of the RZT shell models with Q1, T1 and QT1 irregular mesh schemes with respect to the MSC/NASTRAN 3D reference solution.

Mesh scheme	Regular Quad 16 x 16 ($N_n = 289$)	Regular Tria 16 x 16 ($N_n = 289$)	Irregular Q1 ($N_n = 283$)	Irregular T1 ($N_n = 283$)	Irregular QT1 ($N_n = 283$)
$E\%(\omega_1)$	1.71%	2.78%	6.37%	2.67%	5.16%
$E\%(\omega_2)$	1.25%	2.60%	7.43%	2.35%	5.68%
$E\%(\omega_3)$	1.36%	2.82%	3.65%	2.72%	2.91%
$E\%(\omega_4)$	1.13%	2.50%	4.12%	2.42%	3.22%
$E\%(\omega_5)$	1.25%	2.99%	2.59%	2.38%	2.24%

Table 13. Pinched cap natural frequencies: percent errors of the RZT shell models with Q2, T2 and QT2 irregular mesh schemes with respect to the MSC/NASTRAN 3D reference solution.

Mesh scheme	Regular Quad 32 x 32 ($N_n = 1089$)	Regular Tria 32 x 32 ($N_n = 1089$)	Irregular Q2 ($N_n = 1087$)	Irregular T2 ($N_n = 1087$)	Irregular QT2 ($N_n = 1087$)
$E\%(\omega_1)$	0.76%	1.00%	1.49%	0.83%	1.47%
$E\%(\omega_2)$	0.28%	0.60%	1.06%	0.40%	0.90%
$E\%(\omega_3)$	0.35%	0.67%	0.68%	0.52%	0.64%
$E\%(\omega_4)$	0.36%	0.74%	0.74%	0.63%	0.71%
$E\%(\omega_5)$	0.36%	0.79%	0.55%	0.63%	0.55%

When a reduced number of elements and nodes is used (Table 12), irregular mesh schemes can lead to natural frequencies prediction slightly poorer than those obtained for regular meshes, especially when using Quad elements (Q1 and QT1). The distorted mesh scheme with only Tria elements (T1) is slightly more accurate than the

corresponding regular one with the same number of nodes, revealing that Tria elements can easily adapt to the geometry of the structure even if a regular discretization pattern is not followed. Similar conclusions can be drawn considering the results with finer meshes (Table 13) but, in this case, errors are very low for regular and irregular schemes. These results demonstrate that, also for curved structures and with an adequate level of discretization, the proposed RZT-based shell elements are accurate both with regular and with irregular mesh patterns.

5. CONCLUSIONS

A three-node triangular and a four-node quadrilateral flat shell element based on the Refined Zigzag Theory (RZT) have been developed to study multilayered composite and sandwich curved structures. The theory is reviewed in order to set the framework for the development of the finite elements. RZT is based on seven kinematic variables that include the three displacements, the two bending rotations and the two zigzag rotations. Employing interdependent C^0 -continuous shape functions derived for a beam-frame element eliminates shear locking within a realistic range of edge length-to-thickness ratios and provides the shell element with a displacement field that is fully compatible at the interfaces among adjacent elements. In particular, the “coarse” drilling rotation is introduced through the shape functions and the effect of “zigzag” drilling rotation is artificially added to the stiffness matrix. Moreover, due to the “coarse” drilling degree of freedom formulation, a stabilization matrix has been added to the element stiffness matrix in order to remove zero-energy modes. Full-quadrature integration has been used on all stiffness, mass and load-vector terms to ensure variational consistency and correct stiffness-matrix rank.

The static and dynamic numerical experiments performed on a flat multilayered composite and on a double curved sandwich structure have demonstrated the

convergence characteristics of the new RZT-based shell elements, their robustness with respect to distorted and irregular mesh schemes and the elimination of shear-locking for realistically thin structures (edge length-to-thickness ratios ranging from 10 to 10^4).

Comparisons have been made with the results coming from RZT exact solution (when available), high-fidelity 3D finite element models and a 2D FSDT-based shell element formulation. This novel element technology offers substantial improvements over the current state-of-the-art plate modeling which is either based on FSDT or higher-order plate and continuum solid elements.

Future developments of this effort will include: (i) formulation of shear locking-free finite elements based on both RZT and $\text{RZT}^{(m)}$ for the analysis of extremely thin structures and (ii) through-the-thickness analysis (displacements and stresses) of multilayered curved structures.

Appendix A

The membrane, bending and transverse shear strain measures of RZT are defined as [31]

$$\begin{aligned}\mathbf{e}_m &\equiv \begin{bmatrix} u_{,1} & v_{,2} & (u_{,2} + v_{,1}) \end{bmatrix}^T \\ \mathbf{e}_b &\equiv \begin{bmatrix} \theta_{1,1} & \psi_{1,1} & \theta_{2,2} & \psi_{2,2} & (\theta_{1,2} + \theta_{2,1}) & (\psi_{1,2} & \psi_{2,1}) \end{bmatrix}^T \\ \mathbf{e}_s &\equiv \begin{bmatrix} (w_{,1} + \theta_1) & \psi_1 & (w_{,2} + \theta_2) & \psi_2 \end{bmatrix}^T\end{aligned}\tag{A1}$$

The RZT stiffness coefficients matrices are [31]

$$\begin{aligned}
\mathbf{A} &\equiv \int_{-h}^h \mathbf{C}^{(k)} dz \\
\mathbf{B} &\equiv \int_{-h}^h \mathbf{C}^{(k)} \mathbf{B}_\phi^{(k)} dz \\
\mathbf{D} &\equiv \int_{-h}^h \mathbf{B}_\phi^{(k)T} \mathbf{C}^{(k)} \mathbf{B}_\phi^{(k)} dz \\
\mathbf{G} &\equiv \int_{-h}^h \mathbf{B}_\beta^{(k)T} \mathbf{Q}^{(k)} \mathbf{B}_\beta^{(k)} dz
\end{aligned} \tag{A2}$$

with

$$\begin{aligned}
\mathbf{B}_\phi^{(k)} &\equiv \begin{bmatrix} z & \phi_1^{(k)} & 0 & 0 & 0 & 0 & 0 \\ 0 & 0 & z & \phi_2^{(k)} & 0 & 0 & 0 \\ 0 & 0 & 0 & 0 & z & \phi_1^{(k)} & \phi_2^{(k)} \end{bmatrix} \\
\mathbf{B}_\beta^{(k)} &\equiv \begin{bmatrix} 1 & \beta_1^{(k)} & 0 & 0 \\ 0 & 0 & 1 & \beta_2^{(k)} \end{bmatrix}
\end{aligned} \tag{A3}$$

It is in particular interesting to recall the definition of some coefficients of the matrix \mathbf{G}

$$\begin{aligned}
G_{11} &= \int_{-h}^h Q_{11}^{(k)} dz \\
G_{22} &= \int_{-h}^h \beta_1^{(k)} Q_{11}^{(k)} \beta_1^{(k)} dz \\
G_{33} &= \int_{-h}^h Q_{22}^{(k)} dz \\
G_{44} &= \int_{-h}^h \beta_2^{(k)} Q_{22}^{(k)} \beta_2^{(k)} dz
\end{aligned} \tag{A4}$$

The RZT inertia coefficients matrix is

$$\mathbf{\Gamma} \equiv \begin{bmatrix} \mathbf{I}_0 & 0 & 0 & \mathbf{I}_1 & 0 & \mathbf{I}_0^{\phi_1} & 0 \\ 0 & \mathbf{I}_0 & 0 & 0 & \mathbf{I}_1 & 0 & \mathbf{I}_0^{\phi_2} \\ 0 & 0 & \mathbf{I}_0 & 0 & 0 & 0 & 0 \\ \mathbf{I}_1 & 0 & 0 & \mathbf{I}_2 & 0 & \mathbf{I}_1^{\phi_1} & 0 \\ 0 & \mathbf{I}_1 & 0 & 0 & \mathbf{I}_2 & 0 & \mathbf{I}_1^{\phi_2} \\ \mathbf{I}_0^{\phi_1} & 0 & 0 & \mathbf{I}_1^{\phi_1} & 0 & \mathbf{I}_2^{\phi_1} & 0 \\ 0 & \mathbf{I}_0^{\phi_2} & 0 & 0 & \mathbf{I}_1^{\phi_2} & 0 & \mathbf{I}_2^{\phi_2} \end{bmatrix} \tag{A5}$$

where [9]

$$\begin{aligned}
I_0 &\equiv \int_{-h}^h \rho^{(k)} dz & I_1 &\equiv \int_{-h}^h \rho^{(k)} z dz & I_2 &\equiv \int_{-h}^h \rho^{(k)} z^2 dz \\
I_0^{\phi_1} &\equiv \int_{-h}^h \rho^{(k)} \phi_1^{(k)} dz & I_1^{\phi_1} &\equiv \int_{-h}^h \rho^{(k)} \phi_1^{(k)} z dz & I_2^{\phi_1} &\equiv \int_{-h}^h \rho^{(k)} \left(\phi_1^{(k)}\right)^2 dz \\
I_0^{\phi_2} &\equiv \int_{-h}^h \rho^{(k)} \phi_2^{(k)} dz & I_1^{\phi_2} &\equiv \int_{-h}^h \rho^{(k)} \phi_2^{(k)} z dz & I_2^{\phi_2} &\equiv \int_{-h}^h \rho^{(k)} \left(\phi_2^{(k)}\right)^2 dz
\end{aligned} \tag{A6}$$

Appendix B

The quadratic shape functions P_ℓ used for the initial approximation of deflection in triangular elements, Eq. (16), are defined as follows [54]

$$\begin{aligned}
P_i &\equiv L_i (2L_i - 1) \quad (i = 1, 2, 3) \\
P_{ij} &\equiv 4L_i L_j \quad \begin{pmatrix} i = 1, 2, 3 \\ j = 2, 3, 1 \end{pmatrix}
\end{aligned} \tag{B1}$$

where L_i are the area-parametric coordinates. For quadrilateral elements, P_ℓ are the biquadratic serendipity shape functions [54]

$$\begin{aligned}
P_i &\equiv \frac{1}{4} (1 + \xi_i \xi) (1 + \eta_i \eta) (\xi_i \xi + \eta_i \eta - 1) \quad (i = 1, 2, 3, 4) \\
P_{12} &\equiv \frac{1}{2} (1 - \xi^2) (1 - \eta) \\
P_{23} &\equiv \frac{1}{2} (1 - \eta^2) (1 + \xi) \\
P_{34} &\equiv \frac{1}{2} (1 - \xi^2) (1 + \eta) \\
P_{41} &\equiv \frac{1}{2} (1 - \eta^2) (1 - \xi)
\end{aligned} \tag{B2}$$

where (ξ, η) are the normalized element local in-plane coordinates, $(\xi, \eta) \in [-1, +1]$,

and (ξ_i, η_i) are the coordinates of the i -th corner node.

Quadratic shape functions Q_{1i} and Q_{2i} appearing in the final, “constrained” approximation of deflection (Eq. (18)) are defined as

$$\left. \begin{aligned} Q_{1i} &\equiv \frac{L_i}{2} \left[L_j (x_{1i} - x_{1j}) + L_k (x_{1i} - x_{1k}) \right] \\ Q_{2i} &\equiv \frac{L_i}{2} \left[L_j (x_{2i} - x_{2j}) + L_k (x_{2i} - x_{2k}) \right] \end{aligned} \right\} \begin{cases} i = 1, 2, 3 \\ j = 2, 3, 1 \\ k = 3, 1, 2 \end{cases} \quad (\text{B3})$$

for the triangular element, and as

$$\left. \begin{aligned} Q_{1i} &\equiv \frac{1}{8} \left[P_{ki} (x_{1i} - x_{1k}) + P_{ij} (x_{1i} - x_{1j}) \right] \\ Q_{2i} &\equiv \frac{1}{8} \left[P_{ki} (x_{2i} - x_{2k}) + P_{ij} (x_{2i} - x_{2j}) \right] \end{aligned} \right\} \begin{cases} i = 1, 2, 3, 4 \\ j = 2, 3, 4, 1 \\ k = 4, 1, 2, 3 \end{cases} \quad (\text{B4})$$

for the quadrilateral element, where (x_{1i}, x_{2i}) are the local in-plane coordinates of the i -th corner node and functions P_{ki} and P_{ij} are as defined in Eq. (B2) [52].

Appendix C

For a triangular element it is easy to find that Eq. (31) yields

$$[a_i] = [1/3 \quad 1/3 \quad 1/3] \quad (\text{C1})$$

thus leading to the following expression for matrix $[K^w]$ (Eq. (33))

$$[K^w] = \frac{S}{36} \begin{bmatrix} 2 & -1 & -1 \\ -1 & 2 & -1 \\ -1 & -1 & 2 \end{bmatrix} \quad (C2)$$

with S area of the triangular element.

References

- [1] Liu D, Li. X An overall view of laminate theories based on displacement hypothesis. Journal of Composite Materials, 1996;30(14):1539–1561.
- [2] Reddy JN. Mechanics of laminated composite plates. NewYork:CRC Press, 1997.
- [3] Abrate S, Di Sciuva M. Equivalent single layer theories for composite and sandwich structures: A review. Composite Structures 2017;179:482 – 494.
- [4] Reissner E, Stavsky Y. Bending and stretching of certain types of heterogeneous aeolotropic elastic plates. Journal of Applied Mechanics 1961;28(3):402–408.
- [5] Reissner E, The effect of transverse shear deformation on the bending of elastic plates. Journal of Applied Mechanics 1945;12:68–77.
- [6] Mindlin RD. Influence of rotatory inertia and shear deformation on flexural motions of isotropic elastic plates. Journal of Applied Mechanics 1951;(18):31–38.
- [7] Whitney JM, Pagano NJ. Shear deformation in heterogeneous anisotropic plates. Journal of Applied Mechanics 1970;37(4):1031–1036.
- [8] Ferreira ALM. A formulation of the multiquadratic radial basis function method for the analysis of laminated composite plates. Composite Structures 2003;59:385–392.
- [9] Iurlaro L, Gherlone M, Di Sciuva M, Tessler A. Assessment of the Refined Zigzag Theory for bending, vibration, and buckling of sandwich plates: a comparative study of different theories, Composite Structures 2013;106:777-792.

- [10] Librescu L, Khdeir A, Reddy J. A comprehensive analysis of the state of stress of elastic anisotropic flat plates using refined theories. *Acta Mechanica* 1987;70:57–81.
- [11] Noor AK., Burton WS. Assessment of shear deformation theories for multilayered composite plates. *Applied Mechanics Reviews* 1989;42(1):1–13.
- [12] Reddy JN. A simple higher-order theory for laminated composite plates. *Journal of Applied Mechanics* 1984; 51(4):745–752.
- [13] Pandya B. N., Kant T. Flexural analysis of laminated composites using refined higher order C^0 plate bending elements, *Computational Methods in Applied Mechanical Engineering*, n. 66, 1988, p. 173-198.
- [14] Touratier M. An efficient standard plate theory. *International Journal of Engineering Sciences*, 1991;29:901–916.
- [15] Tessler A. An improved plate theory of {1,2}-order for thick composite laminates. *International Journal of Solids and Structures* 1993;30(7):981 – 1000.
- [16] Kant T, Marur SR, Rao GS, Analytical solution to the dynamic analysis of laminated beams using higher order refined theories, *Composite Structures* 1998;40(1):1-9.
- [17] Cook GM, Tessler A. A {3,2}-order bending theory for laminated composite and sandwich beams. *Composites Part B: Engineering* 1998;29(5):565 – 576.
- [18] Barut A, Madenci E, Anderson T, Tessler A. Equivalent single-layer theory for a complete stress field in sandwich panels under arbitrarily distributed loading. *Composite Structures* 2002;58(4):483 – 495.
- [19] Reddy JN. A generalization of two-dimensional theories of laminated composite plates. *Communications in Applied Numerical Methods* 1987;3(3):173–180.
- [20] Lu X, Liu D. An interlaminar shear stress continuity theory for both thin and thick composite laminates. *Journal of Applied Mechanics* 2002;59(3):502–509.

- [21] Di Sciuva M. Development of an anisotropic, multilayered, shear-deformable rectangular plate element. *Computers & Structures* 1985;21(4):789 – 796.
- [22] Di Sciuva M. Bending, vibration and buckling of simply supported thick multilayered orthotropic plates: An evaluation of a new displacement model. *Journal of Sound and Vibration* 1986;105(3):425 – 442.
- [23] Di Sciuva M. An improved shear-deformation theory for moderately thick multilayered anisotropic shells and plates. *Journal of Applied Mechanics* 1987;54(3):589–596.
- [24] Di Sciuva M. Multilayered anisotropic plate models with continuous interlaminar stresses. *Composite Structures* 1992;22(3):149 – 167.
- [25] Cho M, Parmenter RR. Efficient higher order composite plate theory for general lamination configurations. *AIAA Journal* 1993;31(7):1299–1306.
- [26] Averill RC. Static and dynamic response of moderately thick laminated beams with damage. *Composites Engineering* 1994;4(4):381 – 395.
- [27] Averill RC, Yip YC. Development of simple, robust finite elements based on refined theories for thick laminated beams. *Computers & Structures* 1996;59(3):529–546.
- [28] Icardi U. A three-dimensional zig-zag theory for analysis of thick laminated beams, *Composite structures* 2001;52:123-135.
- [29] Icardi U, Sola F. Development of an efficient zigzag model with variable representation of displacements across the thickness, *Journal of Engineering Mechanics* 2014;140(3):531-541
- [30] Tessler A, Di Sciuva M, and Gherlone M. A refined zigzag beam theory for composite and sandwich beams. *Journal of Composite Materials* 2009;43(9):1051–1081.

- [31] Tessler A, Di Sciuva M, and Gherlone M. A consistent refinement of first-order shear-deformation theory for laminated composite and sandwich plates using improved zigzag kinematics. *Journal of Mechanics of Materials and Structures* 2010;5(2):341–367.
- [32] Tessler A, Di Sciuva M, and Gherlone M. A homogeneous limit methodology and refinements of computationally efficient zigzag theory for homogeneous, laminated composite, and sandwich plates. *Numerical Methods for Partial Differential Equations* 2011;27(1):208–229.
- [33] Iurlaro L, Gherlone M, Di Sciuva M. Bending and free vibration analysis of functionally graded sandwich plates using the refined zigzag theory. *Journal of Sandwich Structures and Materials* 2014;16: 669–699.
- [34] Di Sciuva M, Sorrenti M. Bending and free vibration analysis of functionally graded sandwich plates: an assessment of the refined zigzag theory. *Journal of Sandwich Structures & Materials* 2019:1–43.
- [35] Di Sciuva M, Sorrenti M. Bending, free vibration and buckling of functionally graded carbon nanotube-reinforced sandwich plates, using the extended Refined Zigzag Theory. *Composite Structures* 2019;227:111324.
- [36] Reissner E. On a certain mixed variational theorem and a proposed application. *International Journal for Numerical Methods in Engineering* 1984;20(7):1366–1368.
- [37] Carrera E. Developments, ideas and evaluations based upon Reissner’s mixed variational theorem in the modeling of multilayered plates and shells. *Applied Mechanics Review* 2001;54(4):301–329.
- [38] Murakami H. Laminated composite plate theory with improved in-plane responses. *Journal of Applied Mechanics* 1986;53(3):661–666.

- [39] Toledano A, Murakami H. A composite plate theory for arbitrary laminate configurations. *Journal of Applied Mechanics* 1987;54(1):181–189.
- [40] Tessler A. Refined Zigzag Theory for homogeneous, laminated composite, and sandwich beams derived from Reissner's mixed variational principle. *Meccanica* 2015;50(10):2621–2648.
- [41] Iurlaro L, Gherlone M, Di Sciuva M, Tessler A. Refined Zigzag Theory for laminated composite and sandwich plates derived from Reissner's Mixed Variational Theorem. *Composite Structures* 2015;133:809–817.
- [42] Gherlone M. On the use of zigzag functions in equivalent single layer theories for laminated composite and sandwich beams: a comparative study and some observations on external weak layers. *Journal of Applied Mechanics* 2013;80(6).
- [43] Icardi U, Sola F. Assessment of recent zig-zag theories for laminated and sandwich structures. *Composites Part B: Engineering* 2016;97:26–52.
- [44] Abrate S, Di Sciuva M. Multilayer models for composite and sandwich structures. In: Beaumont PWR, Zweben CH, eds. *Comprehensive Composite Materials II*. Elsevier. 2018:399–425.
- [45] Gherlone M., Tessler A, Di Sciuva M., C^0 beam elements based on the Refined Zigzag Theory for multilayered composite and sandwich laminates. *Composite Structures* 2011;93(11):2282-2294.
- [46] Tessler A, Dong SB. On a hierarchy of conforming Timoshenko beam elements. *Computers & Structures* 1981;14(3-4):335-344.
- [47] Tessler A, Hughes TJR. An improved treatment of transverse shear in the Mindlin-type four-node quadrilateral element. *Computer Methods in Applied Mechanics and Engineering* 1983;39:311-355.

- [48] Tessler A, Hughes TJR. A three-node Mindlin plate element with improved transverse shear. *Computer Methods in Applied Mechanics and Engineering* 1985;50(1):71-101.
- [49] Di Sciuva M, Gherlone M, Iurlaro L, Tessler A. A class of higher-order C^0 composite and sandwich beam elements based on the Refined Zigzag Theory. *Composite Structures* 2015;132:784–803.
- [50] Groh RMJ, Tessler A. 2017 Computationally efficient beam elements for accurate stresses in sandwich laminates and laminated composites with delaminations. *Computer Methods in Applied Mechanics and Engineering* 2017;320:369-395.
- [51] Versino D, Mattone M, Gherlone M, Tessler A, Di Sciuva M. C^0 triangular elements based on the Refined Zigzag Theory for multilayer composite and sandwich plates. *Composites Part B: Engineering* 2013;44(1):218-230.
- [52] Gherlone M. Tria and Quad plate finite elements based on RZT(m) for the analysis of multilayered sandwich structures. *Composite Structures* 2019 220, pp. 510 – 520, 2019.
- [53] Naghdi PM. The Theory of Shell and Plates, *Handbuch der Physik*, VIa.2. Berlin: Springer-Verlag, 1972. p. 425–640.
- [54] Zienkiewicz OC, Taylor RL. The finite element method for solid and structural mechanics. Amsterdam: Elsevier, 2005.
- [55] Dvorkin EN, Bathe KJ. A continuum mechanics based four-node shell element for general nonlinear analysis. *Engineering Computations* 1984;1(1):77–88.
- [56] Belytschko T, Leviathan I. Physical stabilization of 4-node shell element with one-point quadrature. *Computer Methods in Applied Mechanics and Engineering* 1994; 113:321–50.

- [57] Chang-Koon C, Tae-Yeol L. Efficient remedy for membrane locking of 4-node flat shell elements by non-conforming modes. *Computer Methods in Applied Mechanics and Engineering* 2003;192(16–18):1961-1971.
- [58] Wisniewski K, Turska E. Enhanced Allman quadrilateral for finite drilling rotations. *Computer Methods in Applied Mechanics and Engineering* 2006;195(44–47):6086-6109.
- [59] Hughes TJR, Brezzi F. On drilling degrees of freedom. *Computer Methods in Applied Mechanics and Engineering* 1989;72:105–121.
- [60] Ibrahimbegovic A, Taylor RL, Wilson EL. A robust quadrilateral membrane finite element with drilling degrees of freedom. *International Journal for Numerical Methods in Engineering* 1990;30:445-457.
- [61] Hughes TJR, Brezzi F. Dynamic analysis and drilling degrees of freedom, *International Journal for Numerical Methods in Engineering* 1995;38:3193–3210.
- [62] Zhu Y, Zacharia T. A new one-point quadrature, quadrilateral shell element with drilling degrees of freedom. *Computer Methods in Applied Mechanics and Engineering* 1996; 136:165–203.
- [63] Allman DJ. A compatible triangular element including vertex rotations for plane elasticity analysis. *Computers & Structures* 1984; 19:1–8.
- [64] Allman DJ. A quadrilateral finite element including vertex rotations for plane elasticity analysis. *International Journal for Numerical Methods in Engineering* 1988; 26:717–730.
- [65] Cook RD, Further development of a three-node triangular shell element, *International Journal for Numerical Methods in Engineering* 1993;36:1413–1425.

- [66] Cook RD. Four-node “flat” shell element: drilling degrees of freedom, membrane-bending coupling, warped geometry, and behavior. *Computers & Structures* 1994;50:549–555.
- [67] Tessler A. Comparison of interdependent interpolations for membrane and bending kinematics in shear-deformable shell elements. In: *International Conference on Computational Engineering & Sciences*. Los Angeles, 2000.
- [68] Tessler A, Mohr J. A three-node shell element with drilling degrees of freedom for laminated composite and sandwich structures. In: *Fourth International Colloquium on Computation of Shell & Spatial Structures*. Chania, Crete, Greece 2000.
- [69] Neto MA, Leal RP, Yu W. A triangular finite element with drilling degrees of freedom for static and dynamic analysis of smart laminated structures. *Computers & Structures*. 2012;108-109:61-74.
- [70] Mohr JW. An efficient triangular shell finite element for thick composite and sandwich laminates, Bachelor of Science Civil Engineering Thesis, George Washington University, 2000.
- [71] Wisniewski K. *Finite Rotation Shells*. Netherlands: Springer, 2010.
- [72] Ibrahimbegovic A, Frey F. Membrane quadrilateral finite elements with rotational degrees of freedom. *Engineering Fracture Mechanics* 1992;43(1):13–24.
- [73] MacNeal RH, Harder RL. A proposed standard set of problems to test finite element accuracy. *Finite Elements in Analysis and Design* 1985;1:3-20.

Figure captions

Figure 1. Plate geometry and notation for Refined Zigzag Theory.

Figure 2. RZT-based beam finite element: topology and kinematic variables.

Figure 3. Unconstrained RZT-based beam finite element: topology and nodal degrees of freedom.

Figure 4. Constrained RZT-based beam finite element: topology and nodal degrees of freedom.

Figure 5. RZT-based flat shell elements: topology and kinematic variables.

Figure 6. Unconstrained RZT-based flat shell elements: topology and nodal degrees of freedom.

Figure 7. Constrained RZT-based flat shell elements: topology and nodal degrees of freedom.

Figure 8. Regular mesh schemes for $\frac{1}{4}$ of the square plate characterized by N_e = number of subdivisions per edge and N_n = total number of nodes: (a) Quad mesh ($N_e=3$, $N_n=16$), (b) Tria(1) mesh ($N_e=3$, $N_n=16$), (c) Tria(2) mesh ($N_e=3$, $N_n=16$), (a) Tria(3) mesh ($N_e=3$, $N_n=25$).

Figure 9. Square plate problem: convergence of the RZT FEM maximum deflection to the RZT exact one for regular mesh patterns.

Figure 10. Irregular mesh schemes for $\frac{1}{4}$ of the square plate: (a) mesh D1 ($N_n=82$), (b) mesh D2 ($N_n=82$), (c) mesh D3 ($N_n=81$), (d) mesh D4 ($N_n=82$), (e) mesh D5 ($N_n=24$), (f) mesh D6 ($N_n=25$).

Figure 11. Square plate problem: comparison between the performances of the irregular and regular mesh schemes.

Figure 12. Square plate problem: performance of the RZT-shell finite elements for thinner and thinner plates.

Figure 13. Pinched cap geometry ($\frac{1}{4}$ of the structure is represented).

Figure 14. MSC/NASTRAN 3D model of the pinched cap: (a) overview, (b) zoomed view around the hole cutout.

Figure 15. RZT shell model of the pinched cap with 8×8 subdivisions and regular mesh schemes: (a) triangular mesh (128 elements), (b) quadrilateral mesh (64 elements).

Figure 16. Pinched cap static problem: (a) RZT regular Quad shell model (64×64) with applied loads, (b) MSC/NASTRAN 3D model with applied loads.

Figure 17. Irregular mesh schemes for the pinched cap: (a) mesh Q1 ($N_n = 283$), (b) mesh T1 ($N_n = 283$), (c) mesh QT1 ($N_n = 283$), (d) mesh Q2 ($N_n = 1087$), (e) mesh T2 ($N_n = 1087$), (f) mesh QT2 ($N_n = 1087$).